Longitudinal Profiling of Tumor and Immune Compartments Uncovers Patterns of Dysregulation and Associations with Response in Multiple Myeloma

Denis J. Ohlstrom[1,2], William C. Pilcher Jr[1], Marina E. Michaud[2], Chaitanya Acharya[3], Sarthak Satpathy[4], Edgar Gonzalez-Kozlova[5,6], Reyka G. Jayasinghe[7], Katherine Ferguson[1], Hope L. Mumme[4], Shivani Nanda[8,9,10], Yizhe Song[7], Sowmitri Mantrala[4], Dimitra Karagkouni[8,9,10], Jessica Schulman[3], Nick Pabustan[3], Junia Vieira Dos Santos[5,6], Daniel W. Sherbenou[11], Jonathan J. Keats[12], Alexander M. Gout[3], Steven Foltz[3], Alessandro Lagana[5,6], Taxiarchis Kourelis[13], Ravi Vij[14,15], Madhav V. Dhodapkar[16,17], David Avigan[8,9,18], Hearn Jay Cho[3,5,6], Linda B. Baughn[13], Ajay K. Nooka[16], Sagar Lonial[2,19], Shaji Kumar[13], Mehmet K. Samur[20,21], Ioannis S. Vlachos[8,9,10,18,22], Li Ding[7,15], Sacha Gnjatic[5,6,23], George Mulligan[3], and Manoj K. Bhasin[1,2,4]

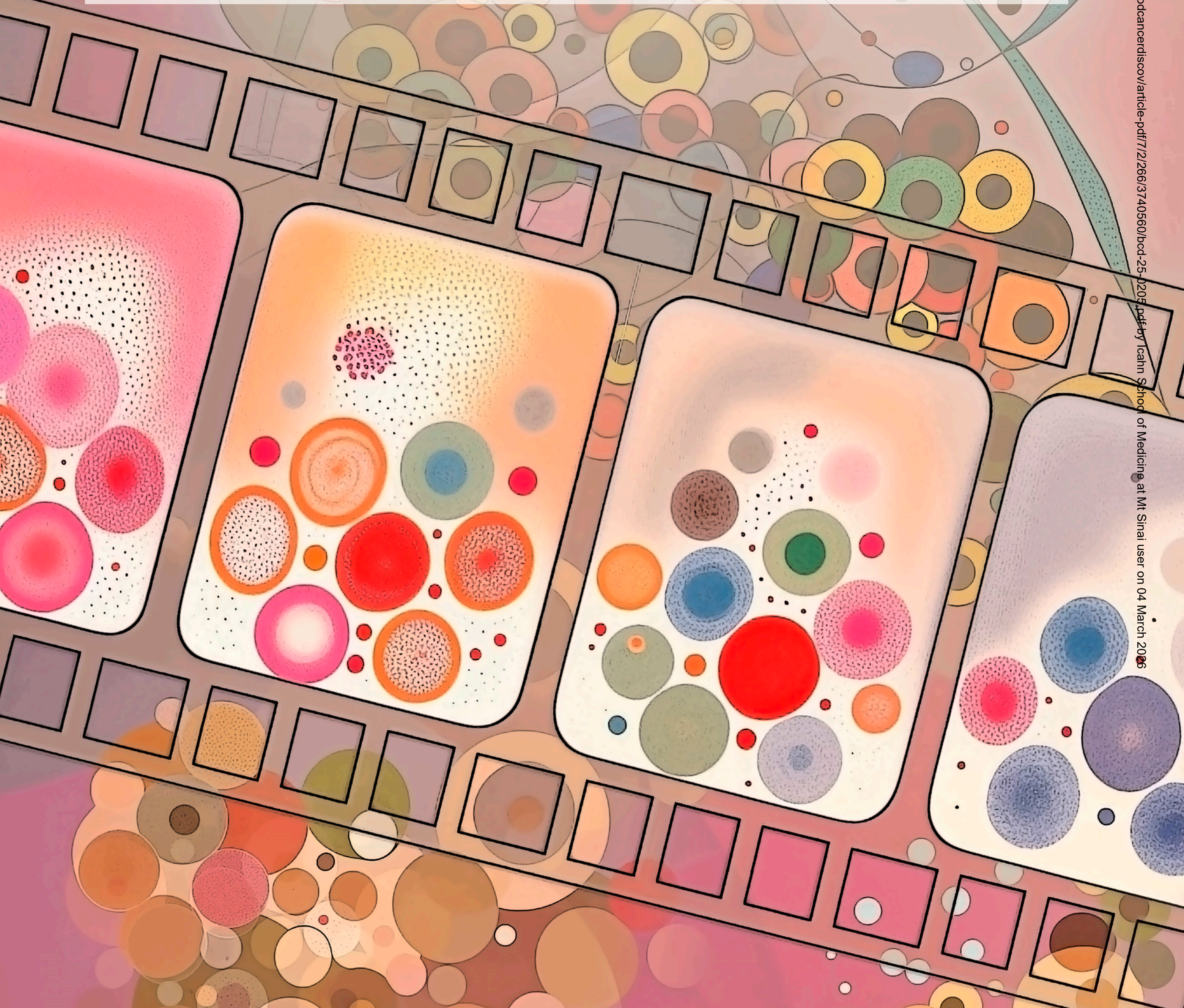

ABSTRACT Multiple myeloma is a malignancy of clonally expanded plasma cells shaped by complex interactions with the immune microenvironment (IME). To investigate immune correlates of treatment response and disease progression, we conducted multi-omics profiling including CD138^{neg} single-cell RNA sequencing of 243 bone marrow samples from 102 patients (631,226 cells) and CD138^{pos} bulk RNA and whole-genome sequencing from 209 samples. In longitudinal analyses, interferon-γ signaling associated with markers of impaired T-cell memory after autologous stem cell transplant, whereas naïve B-cell abundance and immunoglobulin diversity correlated with improved progression-free survival (HR = 0.48; $P = 2.3e^{-4}$). At disease progression, multiple myeloma cells upregulated cancer–testis antigens (CTAg) and immune effector genes, with concurrent B-cell depletion, enrichment of myeloid-derived suppressor cell expression, and phenotypic T-cell exhaustion. These findings highlight dynamic immune–tumor interactions, identifying naïve B-cell reconstitution as a biomarker of durable response and CTAgs as potential targets for high-risk disease at progression.

SIGNIFICANCE: Longitudinal profiling of multiple myeloma and the IME revealed dynamic immune–tumor interactions across the disease course. Altered expression in CD8$^+$ T cells limited memory phenotype after transplant, whereas naïve B-cell recovery associated with sustained treatment response. At progression, CTAg expression associated with immunosuppression, revealing novel mechanisms of immune dysregulation.

INTRODUCTION

Multiple myeloma is an incurable malignancy of clonally expanded plasma cells. Disease incidence has steadily increased over the past 30 years to an estimated 36,000 new diagnoses and 13,000 deaths per year in the United States (1). Advances in multiple myeloma–targeted therapies, autologous stem cell transplantation (ASCT), and immunotherapy have improved 5-year survival rates (2). However, multiple myeloma remains incurable, with most patients ultimately experiencing disease progression (3, 4). Several features contribute to multiple myeloma's response to therapy, including cytogenetics, intratumoral heterogeneity, and composition of the bone marrow (BM) immune microenvironment (IME; refs. 5, 6). In our recent analysis of baseline BM samples from newly diagnosed patients with multiple myeloma in the Multiple Myeloma Research Foundation (MMRF) Immune Atlas, we identified immune alterations associated with rapid disease progression—namely reduced B-cell abundance, expanded myeloid populations, and a shift toward terminally differentiated cytotoxic T cells—that remained prognostic even after adjusting for cytogenetics and patient demographics (bioRxiv 2024.05.15.593193v1). However, the dynamics of the IME through treatment and interplay between plasma cells and the IME during disease progression remains incompletely understood.

Recent studies have uncovered quantitative abundance changes in the IME along with alterations in gene expression associated with the progression of multiple myeloma (7, 8). Key pathologic features of the IME include the development of dysfunctional T cells, accumulation of myeloid-derived

---

[1]Coulter Department of Biomedical Engineering, Georgia Institute of Technology, Atlanta, Georgia. [2]Department of Pediatrics, Emory School of Medicine, Atlanta, Georgia. [3]MMRF, Norwalk, Connecticut. [4]Department of Biomedical Informatics, Emory School of Medicine, Atlanta, Georgia. [5]Department of Immunology and Immunotherapy, Tisch Cancer Institute, Icahn School of Medicine at Mount Sinai, New York, New York. [6]Department of Genetics and Genomic Sciences, Tisch Cancer Institute, Icahn School of Medicine at Mount Sinai, New York, New York. [7]Department of Medicine, Washington University in St. Louis, St. Louis, Missouri. [8]Beth Israel Deaconess Medical Center, Boston, Massachusetts. [9]Harvard Medical School, Boston, Massachusetts. [10]Broad Institute of MIT and Harvard, Cambridge, Massachusetts. [11]University of Colorado Anschutz Medical Campus, Aurora, Colorado. [12]Integrated Cancer Genomics Division, Translational Genomics Research Institute, Phoenix, Arizona. [13]Mayo Clinic, Rochester, Minnesota. [14]Siteman Cancer Center, Washington University in St. Louis, St. Louis, Missouri. [15]Bone Marrow Transplantation & Leukemia Section, Division of Oncology, Washington University School of Medicine, St. Louis, Missouri. [16]Department of Hematology Oncology, Emory School of Medicine, Atlanta, Georgia. [17]Winship Cancer Institute, Emory School of Medicine, Atlanta, Georgia. [18]Cancer Center & Cancer Research Institute, Beth Israel Deaconess Medical Center, Boston, Massachusetts. [19]Aflac Cancer and Blood Disorders Center, Children's Healthcare of Atlanta, Atlanta, Georgia. [20]Department of Biostatistics, Harvard T. H. Chan School of Public Health, Boston, Massachusetts. [21]Department of Data Science, Dana-Farber Cancer Institute, Boston, Massachusetts. [22]Spatial Technologies Unit, Harvard Medical School Initiative for RNA Medicine, Boston, Massachusetts. [23]Human Immune Monitoring Center, Department of Immunology and Immunotherapy, Tisch Cancer Institute, Icahn School of Medicine at Mount Sinai, New York, New York.

Corresponding Author: Manoj K. Bhasin, Department of Pediatrics, Emory School of Medicine, Health Sciences Research Building, Room N320, 170 Haygood Drive, Atlanta, GA, 30322. E-mail: manoj.bhasin@emory.edu

Blood Cancer Discov 2026;7:266–86

doi: 10.1158/2643-3230.BCD-25-0205

suppressor cells (MDSC), and depletion of B cells (7, 9). Treatment with ASCT and pretransplant conditioning with high-dose cytotoxic agents induces profound depletion and alteration of the IME, creating a period of suboptimal immune surveillance while the immune system reconstitutes. Previous studies have described patient-specific differences in the IME's response after ASCT and its relationship with the duration of response using flow cytometry (10), mass cytometry (9), and single-cell RNA sequencing (scRNA-seq; ref. 11). Even after reconstitution, multiple myeloma cells persist and dysregulate the IME through several mechanisms, including direct alteration of the IME via secretion of soluble factors, indirect alteration by recruitment of immunosuppressive cell types, evasion by decreased expression of immunoreactive epitopes, and overcoming the IME by aberrant proliferative and antiapoptotic pathways (12–15). However, the dynamics of these features through the multiple myeloma disease course require additional study. Longitudinal evaluation of both multiple myeloma and IME-specific features through disease and treatment stages has the potential to reveal critical insights into the mechanisms by which multiple myeloma overcomes the IME.

To this end, we longitudinally evaluated multiple myeloma and the IME at disease onset, response after therapy, and disease progression in patients from the MMRF CoMMPass study (NCT01454297). To facilitate a comprehensive characterization of the disease course, we generated a single-cell profile of 243 CD138^{neg} BM samples collected at disease diagnosis, response, or progression from 102 patients. Combining the analysis of this IME scRNA-seq data with bulk RNA and whole-genome sequencing data from the malignant CD138^{pos} compartment enabled deep characterization to identify IME features associated with treatment response and transcriptomic alterations present in multiple myeloma cells that persist through treatment and lead to disease progression.

RESULTS

Characteristics of Longitudinal Multiple Myeloma Cohort: Clinical and Single-Cell Landscape

To evaluate the dynamics of the IME through the multiple myeloma disease course, we generated and analyzed single-cell profiles for the CD138^{neg} fraction of 243 CD138 sorted BM aspirates from 102 patients with longitudinal samples collected as a part of the CoMMpass Immune Atlas initiative (Fig. 1A). The longitudinal sample cohort was broadly representative of the clinical characteristics of the CoMMpass cohort (n = 1,143). The longitudinal cohort had comparable distributions of age at diagnosis (longitudinal cohort mean = 61.6 years, CoMMpass mean = 62.9 years, $P = 0.29$), sex (60.4% vs. 60.4% male, $P = 1$), and International Staging System (ISS) stage at diagnosis (stage I: 34.3% vs. 35.1%, stage II: 39.2% vs. 35.1%, stage III: 26.5% vs. 29.8% $P = 0.38$, Supplementary Fig. S1A–S1C). There was also comparable composition of cytogenetic groups (e.g., 1q21 gain: 35.6% vs. 38.1%, $P = 0.78$, 17p13 deletion: 10.1% vs. 10.3%, $P = 1$) and the International Myeloma Working Group (IMWG)-defined risk category (29.9% vs. 26.3% high risk, $P = 0.55$; Fig. 1B; Supplementary Fig. S1D; ref. 16). The majority of patients in both cohorts received triplet first-line therapy, though the longitudinal cohort was more homogenous with 85.3% receiving a proteasome inhibitor (PI), immunomodulatory drug (IMiD), and steroid, 12.7% of patients receiving doublet therapy, and 1% receiving chemotherapy, PI, and steroid. By comparison, 44.3% of patients in the CoMMpass cohort received PI, IMiD, and steroid, 16.7% chemotherapy, IMiD, and steroid, and 1.5% PI, chemotherapy, IMiD, and steroid. There was a higher rate of ASCT as first-line therapy for the longitudinal cohort as compared with CoMMPass (67.6% vs. 49.6%; $P = 4.6e^{-4}$; Supplementary Fig. S1E and S1F). Progression-free survival (PFS; $P = 0.82$) and overall survival (OS; $P = 0.21$) were equivalent between the longitudinal and CoMMpass cohorts (Supplementary Fig. S1G and S1H). Of the 102 patients with longitudinal samples, 53 had samples collected at baseline and first response, 51 had samples collected at baseline and first progression, nine of which had longitudinal samples from baseline, first response, and first progression, and 15 patients had samples taken at second/third responses/progressions (Fig. 1C). Thus, our longitudinal cohort provides a large and diverse representative sample of multiple myeloma to evaluate the IME characteristics through multiple myeloma disease stages.

scRNA-seq generated profiles of 631,226 high-quality cells after quality control and doublet filtering from the CD138^{neg} fraction of 243 sorted BM aspirates (Fig. 1D). Cells were annotated into different cell types and states using cell type canonical marker expression information adopted from the cell annotation dictionary prepared as part of the recent Immune Atlas study (bioRxiv 2024.05.15.593193v1; Fig. 1E). The IME of the longitudinal samples were composed of 51.8% T cells, 7.8% NK cells, 12.3% B cells, 13% myeloid cells, 8.1% erythroid cells, and 1.4% other small clusters (e.g., hematopoietic stem cells and mast cells, Supplementary Fig. S2A). To assess the distribution of cell types across disease stages and patients, we calculated the per-cell type entropy and found that all disease stages and patients were well represented among cell types, indicating patient and disease stage–specific cell types were not present (Supplementary Fig. S2A–S2D). In addition to the expected immune populations and despite the use of the CD138^{neg} fraction, 5.6% of cells were annotated as plasma cells. Samples with a greater percentage of plasma cells detected by presorting flow cytometry also had a higher percentage of plasma cells in CD138^{neg} scRNA-seq after CD138-based sorting (R = 0.76; $P = 2.2e^{-16}$; Supplementary Fig. S2E). Furthermore, the inferred copy number state of the plasma cells overlapped with the alterations detected in whole-genome sequencing (Supplementary Fig. S3A–S3F), indicating that most of the plasma cells were malignant. This suggests that samples with high myeloma loads may have experienced cell flow through the CD138 selection column due to the saturation of its capacity.

After annotating broad cell types, we further subclustered cells and annotated them based on characteristic gene expression for specific classes (e.g., naïve, memory, and effector) and functional markers [e.g., NFKB and interferon (IFN) response]. The T and NK cell compartment was divided into 11 CD4$^+$ subclusters, 15 CD8$^+$ subclusters, and four NK subclusters (Supplementary Fig. S4A–S4E). The B compartment was

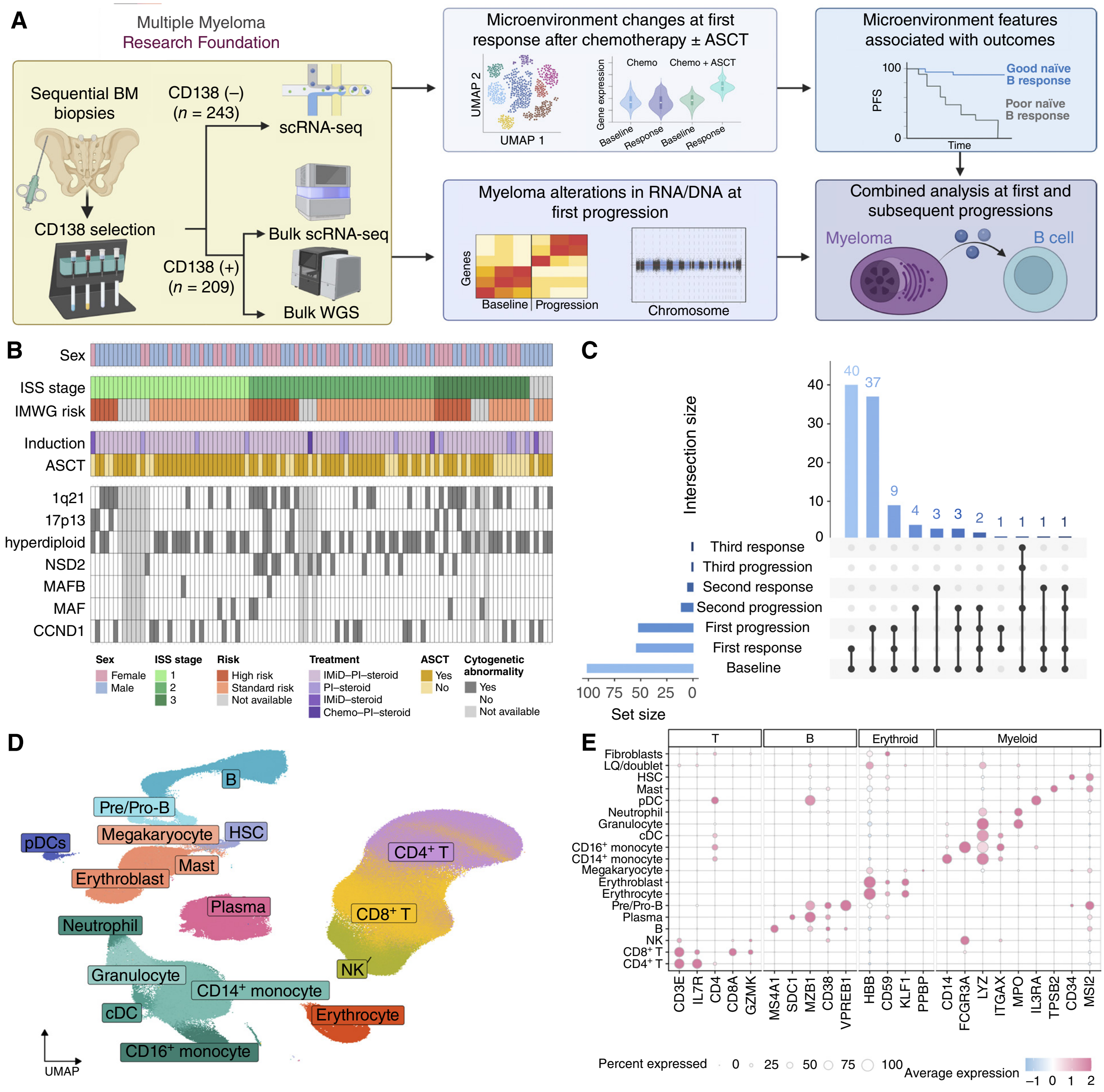

Figure 1. Longitudinal sample scRNA-seq of the IME in multiple myeloma. **A,** Schematic overview of longitudinal CD138^{neg} scRNA-seq and CD138^{pos} bulk RNA and whole-genome sequencing analyses of multiple myeloma. **B,** Tile plot of clinical and genetic features of the 102 patients with longitudinal samples in the CoMMpass scRNA-seq cohort. **C,** Upset plot displaying the number of patients with combinations of samples across baseline and first, second, or third responses and progressions. **D,** UMAP embeddings for the 631,226 cells (243 samples from 102 patients) after quality filtering and doublet removal. **E,** Dot plot of canonical cell type genes. Dot color indicates average normalized, scaled expression with blue for low values and pink for high values. cDC, conventional dendritic cell; HSC, hematopoietic stem cell; pDC, plasmacytoid dendritic cell; UMAP, Uniform Manifold Approximation and Projection; WGS, whole-genome sequencing. [**A,** Created in BioRender. Ohlstrom, D. (2025) https://app.biorender.com/illustrations/69934775230d7098b7c6b7a4]

divided into eight subclusters spanning from pre/pro B to memory B cells (Supplementary Fig. S5A and S5B). The myeloid compartment was divided into 14 subclusters, including monocytes, macrophages, neutrophils, and progenitors (Supplementary Fig. S5C and S5D). This high-resolution analysis enabled the identification of both canonical and rare immune cell populations within the BM, providing a comprehensive cellular framework for downstream correlation with disease progression and response to therapy.

Induction with ASCT Induces Alterations in B and T Cells Not Observed with Induction Therapy Alone

To evaluate how first-line multiple myeloma treatment impacts the IME, we compared the cellular composition and gene expression of CD138^{neg} scRNA-seq in longitudinal BM aspirates from baseline and first response (Fig. 2A). Twenty-two patients had biopsies taken after induction, 26 patients had biopsies taken after ASCT (following induction), and five patients had biopsies taken at both time points.

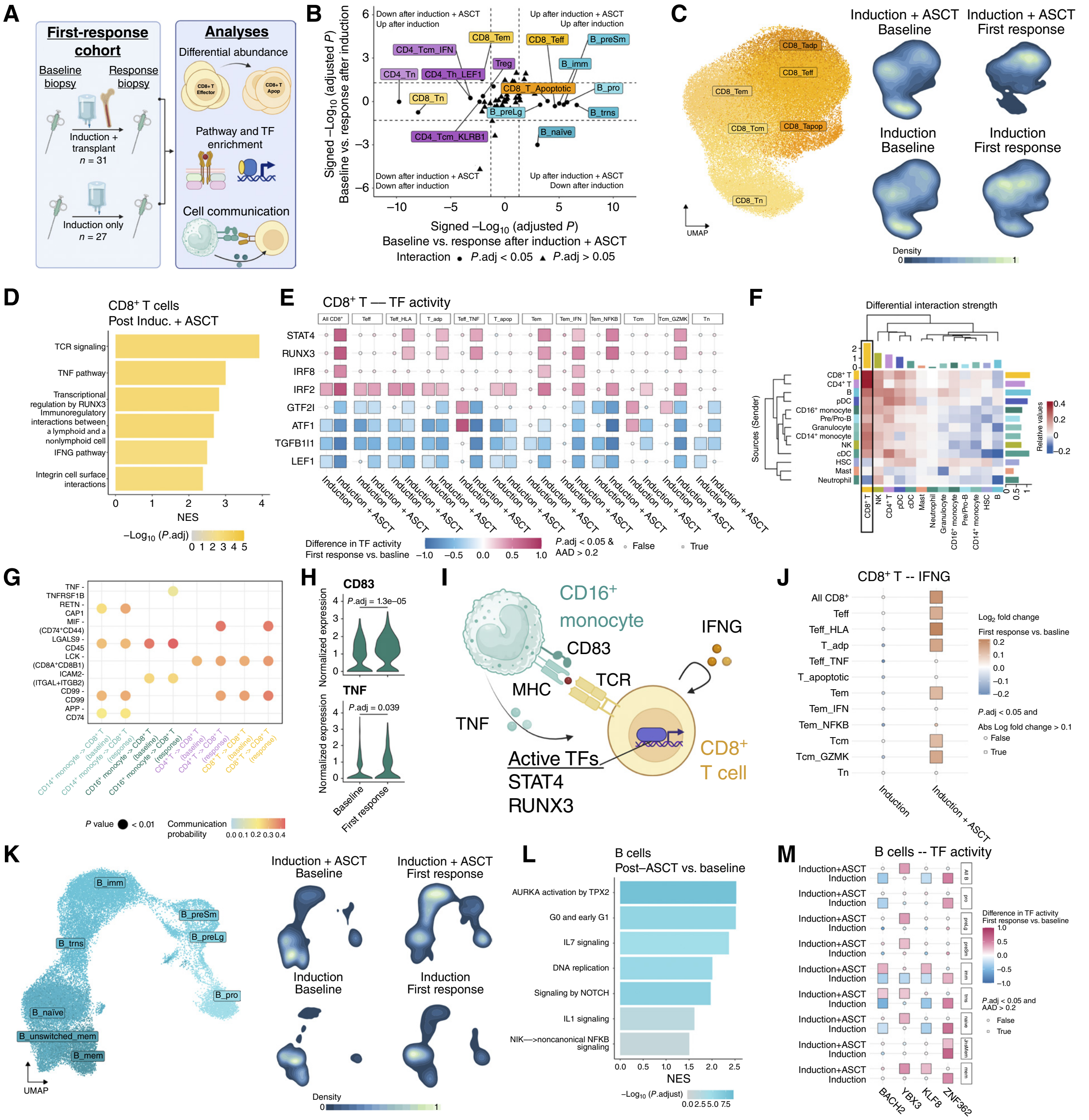

Figure 2. Induction therapy and ASCT induces compositional alterations in the B and T compartments not observed with induction therapy alone. **A,** Schematic overview of the analyses performed. Thirty-one patients had longitudinal baseline and first response after induction with ASCT, and 27 patients had baseline and first response post-induction samples. **B,** Dot plot displaying the changes in immune cell subcluster proportion from baseline to first response after induction on the *Y* axis and from baseline to first response after induction and ASCT on the *X* axis. A linear mixed effect model was used to compare subcluster proportions, and changes were considered significant based on multiple comparisons adjusted *P* value (*P*.adj) < 0.05 for interaction between time and treatment (i.e., the change from baseline to first response was different in the induction and induction with ASCT groups) and an *P*.adj < 0.05 by Tukey *post hoc* testing (i.e., the change from baseline to first response was significant in at least one of the treatment groups). **C,** UMAP embeddings for CD8$^+$ T cells and corresponding density plots displaying the normalized density of cells. **D,** Bar plot of GSEA of CD8$^+$ T effector cells comparing post-ASCT response with baseline. **E,** Heatmap of differential TF activity comparing first response to baseline calculated using decoupleR. decoupleR uses a univariate linear model to calculate activity of a TF based on the expression of known downstream genes, with positive values indicating relatively high activity and negative values relatively decreased activity. *P* values were computed using a variance-overestimated *t* test to limit false positive results. **F,** Heatmap depicting the difference in interaction strength between immune cells at first-response post-ASCT vs. baseline as calculated by CellChat. **G,** Dot plot of pathways with differential communication probability between first response post-ASCT and baseline. **H,** Violin plots of gene expression in CD16$^+$ monocytes. Differential expression was executed using limma–voom with Benjamini–Hochberg multiple comparisons correction. **I,** Schematic synopsis of potential interactions between CD16$^+$ monocytes and CD8$^+$ T cells. **J,** Heatmap displaying the log$_2$ fold change of *IFNG* expression comparing first response to baseline in CD8$^+$ T cells. *P* values and fold changes calculated as in (**H**). **K,** UMAP embeddings for B cells and corresponding density plots displaying the normalized density of cells as in (**C**). **L,** Bar plot of GSEA of B cells comparing post-ASCT response with baseline. **M,** Heatmap of TF activity in B cells calculated using decoupleR as in (**E**). cDC, conventional dendritic cell; Induc., induction; pDC, plasmacytoid dendritic cell; UMAP, Uniform Manifold Approximation and Projection. [**A,** Created in BioRender. Ohlstrom, D. (2025) https://app.biorender.com/illustrations/699347d4e198ad025ed50daa]

Postinduction biopsies were taken at a median of 112 days after diagnosis, and post-induction and post-ASCT biopsies were taken at a median of 272 days after diagnosis and 99 days after ASCT (Supplementary Fig. S6A). Comparing the clinical characteristics from the cohort of patients who had first-response samples after induction to those after induction and ASCT, the induction group was older on average (induction average age at diagnosis = 63.3 years, induction and ASCT = 55.6 years, $P = 0.036$), had a lower percentage of males (57.6% vs. 72.7%, $P = 0.045$), and comparable distributions of ISS stage ($P = 0.73$) and IMWG risk ($P = 0.80$; Supplementary Fig. S6B–S6E). The majority of patients in both cohorts received PI, IMID, and steroid-based induction therapy ($P = 0.8$; Supplementary Fig. S6F).

Given that ASCT is associated with profound disruption of the IME (9), we hypothesized that compositional changes would be observed to a greater extent after induction and ASCT as compared with after induction alone. Consistent with previous reports (10, 17), at the broad cell type level, cellular proportion analysis depicted a significant increase after ASCT in B cells [log$_2$ fold proportion (L$_2$FP) = 0.93, adjusted P, P.adj = 1.3e^{-4}) and pre/pro B cells (L$_2$FP = 1.75, P.adj = 2.1e^{-7}) as well as depletion of CD4$^+$ T cells (L$_2$FP = −1.2, P.adj = 3.8e^{-10}, Supplementary Fig. S7A–S7F). Strikingly, cellular proportion analysis at the subcluster level identified 15 subclusters from the B and T compartments that uniquely changed from baseline to first response after ASCT, whereas only two subclusters had significant changes from baseline to first response that were unique to induction only (Fig. 2B; Supplementary Fig. S8A–S8E). These findings indicate that the IME undergoes several compositional shifts at 100 days after ASCT that are not observed after induction with PI-based therapies alone. To further characterize the pathways and interactions driving changes in the T-cell compartment, we next performed a focused analysis of its composition and gene expression.

IFN-γ and TNF Support CD8$^+$ T Bias toward Apoptosis over Memory Phenotype in the Post-ASCT IME

Comparison of the proportion of T subclusters from baseline to first response after ASCT revealed a shift toward an inflammatory IME not observed after induction alone. As expected, naïve CD4$^+$ (L$_2$FP = −1.84, P.adj = 1.7e^{-10}) and CD8$^+$ (L$_2$FP = −1.93, P.adj = 9.9e^{-9}) T cells were significantly depleted, likely reflecting delayed reconstitution due to age-related thymic involution (18, 19). Consistent with an inflammatory IME, cytotoxic CD8$^+$ T effector cells were significantly expanded after ASCT (L$_2$FP = 1.35, P.adj = 2.4e^{-5}) whereas immunosuppressive T regulatory cells were significantly reduced (L$_2$FP = −0.7, P.adj = 9.5e^{-3}, Supplementary Fig. S8D and S8E). Notably, CD8$^+$ T effector seemed to be biased toward apoptosis over effector memory phenotype, with early apoptotic CD8$^+$ effector T cells depicting significant increase after ASCT (L$_2$FP = 1.57, P.adj = 1.1e^{-4}), whereas CD8$^+$ effector memory T cells were significantly decreased (L$_2$FP = −0.94, P.adj = 8e^{-3}; Fig. 2C; Supplementary Fig. S8D and S8E). To investigate the mechanisms driving the bias away from effector memory phenotype, we next characterized signaling pathways within and between immune populations that influence CD8$^+$ effector T-cell fate in the post-ASCT IME.

To investigate the transcriptional programs underlying the expansion of effector CD8$^+$ T cells and their bias toward apoptosis over effector memory phenotype, we compared the gene expression profiles of CD8$^+$ T cells following ASCT versus induction alone. Differential expression and gene set enrichment analysis (GSEA) identified several effector-promoting pathways, including increased tumor necrosis factor (TNF) signaling [normalized enrichment score (NES) = 3, P.adj = 8.6e^{-4}] and IFN-γ signaling (NES = 2.51, P.adj = 1.5e^{-3}; Fig. 2D) that were not found after induction only (Supplementary Fig. S9A). Notably, IFN-γ signaling has been shown to drive CD8$^+$ effector T cells toward apoptosis (20, 21), aligning with our observation of increased early apoptotic effectors after ASCT. Transcription factor (TF) analysis further identified enrichment for several TFs downstream of IFN-γ stimulation, including STAT4 [average activity difference (AAD) = 0.70, P.adj = 1e^{-250}] and RUNX3 (AAD = 0.73, P.adj = 1e^{-250}; Fig. 2E).

Given that GSEA identified enrichment in CD8$^+$ T cells for interaction with a nonlymphoid cell (NES = 2.68, P.adj = 8.6e^{-4}), we next performed differential cell communication analysis (22) to identify potential intracellular signals influencing T-cell fate. This analysis revealed that CD8$^+$ effector T cells had the highest incoming signal strength after ASCT (Fig. 2F), in contrast to only moderate incoming signaling following induction alone (Supplementary Fig. S9B). Examining the differentially active pathways between baseline and post-ASCT response, we found TNF signaling between CD16$^+$ monocytes and CD8$^+$ T cells was significant only in the post-ASCT samples ($P < 0.01$; Fig. 2G; Supplementary Fig. S9C), suggesting a monocytic contribution to the inflammatory state of CD8$^+$ T cells. Given TNF's dual role in promoting effector function and driving apoptosis during sustained activation (23), this signaling axis likely contributes to the skewing of CD8$^+$ T cells toward apoptosis over memory phenotype.

Together, the GSEA and cell communication analyses highlight a multifaceted mechanism shaping the CD8$^+$ T-cell compartment after ASCT. Compared with baseline samples, CD16$^+$ monocytes exhibit increased TNF [log2 fold change (L$_2$FC) = 0.18, P.adj = 0.039) corresponding with the enriched TNF signaling observed in CD8$^+$ T cells and supporting a shift toward early-apoptotic gene expression (Fig. 2D, H, and I). Corresponding with the enriched T cell receptor (TCR) signaling observed in CD8$^+$ T cells, CD16$^+$ monocytes also have increased expression of *CD83* (L$_2$FC = 0.38, P.adj = 1.3e^{-5}) which supports MHC stability (24). In parallel, CD8$^+$ effector T cells displayed increased expression of *IFNG* (L$_2$FC = 0.20, P.adj = 1.2e^{-70}), consistent with an autocrine or paracrine loop sustaining *IFNG* driven inflammatory signaling and the observed pathway and TF enrichment (Fig. 2I and J). Collectively, these findings suggest that reciprocal interactions between activated myeloid cell and T-cell populations in the post-ASCT BM foster a hyperinflammatory environment that promotes expansion of effector CD8$^+$ T cells and may bias them toward apoptosis rather than durable memory phenotype in multiple myeloma. Targeting key inflammatory mediators such as *IFNG* and *TNF* may offer therapeutic opportunities to restore immune balance and enhance immune function following ASCT.

Post-ASCT B-cell Reconstitution Is Supported by Pro-Proliferative Gene Expression

In addition to the changes observed in the T-cell compartment, six B-cell subclusters were significantly expanded following ASCT but not after induction therapy alone (Fig. 2B). ASCT significantly enhanced pro-B ($L_2FP = 1.5$, $P\text{.adj} = 1.8e^{-6}$), large pre-B ($L_2FP = 1.47$, $P\text{.adj} = 4.5e^{-4}$), small pre-B ($L_2FP = 2.2$, $P\text{.adj} = 3.7e^{-6}$), immature B ($L_2FP = 9.7e^{-6}$), transitional B ($L_2FP = 2.11$, $P = 2.4e^{-7}$), and naïve B ($L_2FP = 1.1$, $P\text{.adj} = 9.9e^{-4}$) populations. These changes were not observed in the induction-only cohort (Fig. 2B; Supplementary Fig. S8), suggesting that ASCT—rather than induction alone—promotes active B-cell repopulation.

To investigate the underlying mechanisms of this expansion, we examined the transcriptional profiles of B-cell subpopulations after ASCT (Fig. 2K). Differential gene expression and GSEA revealed enrichment of pro-proliferative pathways, including aurora kinase A (AURKA) activation by TPX2 (NES = 2.53, $P\text{.adj} = 6.1e^{-9}$) and DNA replication (NES = 2, $P\text{.adj} = 7.6e^{-6}$), as well as pro-activation/differentiation pathways such as NOTCH signaling (NES = 2, $P\text{.adj} = 7.6e^{-6}$) and noncanonical NF-KB signaling (NES = 1.5, $P\text{.adj} = 0.026$, Fig. 2L). These transcriptomic programs suggest coordinated proliferation and maturation of the B-cell compartment after ASCT. Supporting the GSEA findings, TF analysis found that post-ASCT B-cells sustained levels of BACH2 activity, a known driver of B-cell development (25), whereas post-induction B cells had decreased BACH2 activity (AAD = −0.38; $P\text{.adj} = 2.6e^{-34}$; Fig. 2M). Moreover, immature (AAD = 0.29; $P\text{.adj} = 3.2e^{-50}$) and memory (AAD = 0.26; $P\text{.adj} = 2.7e^{-5}$) B cells were enriched for KLF8 activity, a TF associated with cell-cycle progression (26). These transcriptional shifts underscore the presence of a proliferative B compartment following ASCT that may help drive effective B-cell reconstitution.

Patients with Longer-than-Median PFS after ASCT Have a More Robust B-cell Recovery

Next, we aimed to evaluate the association between post-ASCT changes in the IME and the duration of clinical response to determine whether specific immune subpopulations induced by ASCT are linked to improved outcomes. To achieve this goal, we stratified the 31 patients with baseline and post-ASCT first-response samples based on whether their PFS was greater than or less than the median (1,491 days). Samples were annotated as either greater than the median PFS (GMpfs, $n = 15$) or less than the median PFS (LMpfs, $n = 9$), with seven censored before the median PFS (Fig. 3A; Supplementary Fig. S10A–S10D). To determine whether tumor burden influenced IME composition in this analysis, we compared plasma cell percentage from flow cytometry at baseline and after ASCT. At the post-induction, pre-ASCT time point the proportional decrease in involved immunoglobulin (Ig) from baseline was used as a surrogate measure of tumor involvement, as flow cytometry data were not available at this time point. We found no difference in plasma cell percentage at baseline between the LMpfs and GMpfs groups (median plasma % in GMpfs = 15.7%, LMpfs = 14.9%, $P = 0.48$, Supplementary Fig. S10E). Both groups had comparable decreases in involved Ig after induction therapy (median percentage of diagnostic value in GMpfs = 9.2%; LMpfs = 15.5%; $P = 0.95$; Supplementary Fig. S10F). Both groups had near 0% plasma cells after ASCT (median plasma percentage of 0.1% in both groups, $P = 0.59$, Supplementary Fig. S10G), cumulatively indicating that plasma cell burden did not confound analysis of IME composition. Differential abundance analysis of the proportion of broad immune cell types between PFS groups found no differences in change from baseline that are unique to either group (Supplementary Fig. S11A–S11D). However, subcluster analysis depicted that patients with GMpfs had a nearly 4-fold increase in naïve B cells ($L_2FP = 1.96$, $P\text{.adj} = 8.6e^{-4}$) that was not observed in the LMpfs group ($L_2FP = 0.19$; $P\text{.adj} = 0.79$; Fig. 3B and C). The enrichment of naïve B cells in GMpfs patients may reflect more robust immune reconstitution after ASCT, an immunologic feature notably lacking in patients with shorter PFS.

To characterize the transcriptomic changes associated with the high naïve B-cell proportion in GMpfs patients, we compared the expression of naïve B cells at first response between the GMpfs and LMpfs groups. Naïve B cells in GMpfs were found to have enrichment of activation/survival signals (CD40 pathway: NES = 1.92, $P\text{.adj} = 1.7e^{-3}$, MAPK pathway: NES = 1.64, $P\text{.adj} = 4.8e^{-4}$) and migratory pathways (CCR chemokine receptor binding: NES = 1.65, $P\text{.adj} = 3.5e^{-3}$, CXCR receptor binding: NES = 1.81, $P\text{.adj} = 3e^{-3}$; Fig. 3D). Based on these findings, we posited that the relative abundance, activation, and migration of naïve B cells in GMpfs patients would promote activity in developmentally downstream B subtypes as well. Comparing the memory B cells between GMpfs and LMpfs patients, we observed enrichment for germinal center formation (NES = 1.86, $P\text{.adj} = 2.5e^{-3}$), isotype switching (NES = 1.52, $P\text{.adj} = 6.7e^{-3}$), and activation (NES = 1.45, $P\text{.adj} = 3.2e^{-5}$) pathways, suggesting that a large pool of naïve B cells enabled generation of a diverse Ig repertoire. To assess the potential relationship of abundant naïve B cells supporting diverse Ig expression, we calculated the Shannon diversity index on Ig gene expression in the B cells that undergo isotype switching (i.e., naïve to memory cells). The analysis showed that the proportion of naïve B cells is significantly positively associated with the Ig gene Shannon diversity index (R = 0.45; $P = 0.012$; Fig. 3E). Thus, increased naïve B-cell proportion, transcriptional activation, and migratory capacity seem to collectively contribute to a more diverse Ig repertoire in patients with extended post-ASCT remission.

Given that a high proportion of naïve B cells after ASCT was associated with greater than median PFS and increased diversity of Ig gene expression, we next aimed to determine whether post-ASCT serum Ig measurements were also associated with patient outcomes. Using the CoMMpass single-cell Immune Atlas dataset, we randomly split the 408 patients who underwent ASCT, while ensuring equal distribution of ISS stage, into derivation ($n = 205$) and validation ($n = 203$) cohorts (Supplementary Fig. S12A). The resulting derivation and validation cohorts had comparable distributions of clinical features, including age, body mass index, IMWG risk, sex, and induction therapy (all $P > 0.05$, Supplementary Fig. S12A). The optimal Shannon index cut point was calculated from the derivation cohort using the CutP method and found to be a Shannon index value of 0.768. The cut point was applied to both the derivation and validation cohorts,

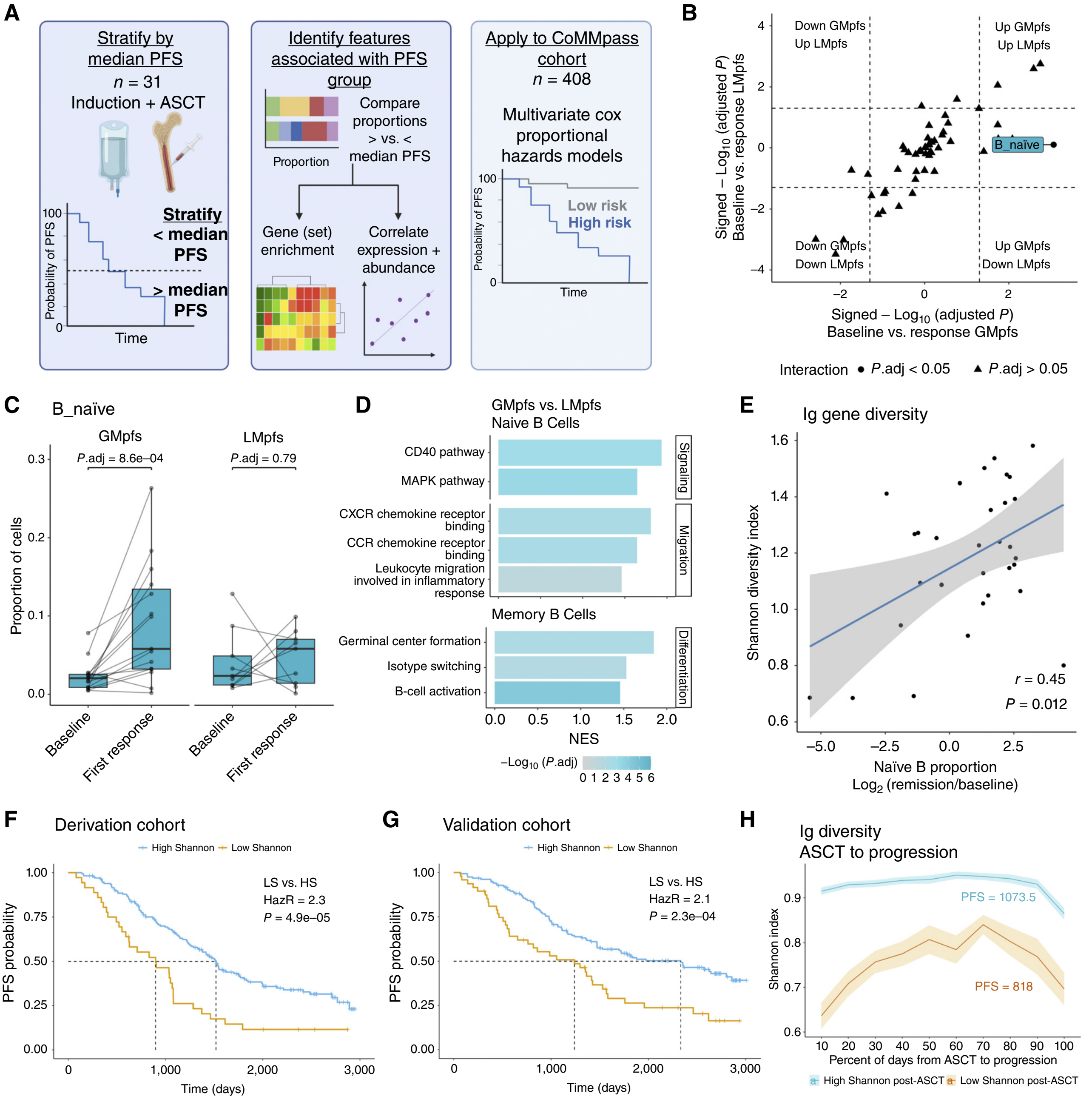

Figure 3. Patients with longer than median PFS after ASCT have a more robust B-cell recovery. **A,** Schematic representation of analyses performed. Thirty-one patients with longitudinal baseline and first-response post-ASCT samples were split into GMpfs ($n = 15$) and LMpfs ($n = 9$), with seven patients censored prior to median PFS. Cell type proportions and expression were compared between GMpfs and LMpfs to examine what changes in the IME associate with clinical outcomes. **B,** Dot plot displaying the increases and decreases in immune cell subcluster proportion from baseline to first response after ASCT in the LMpfs group on the *Y* axis and from baseline to first response post ASCT for the GMpfs group on the *X* axis. A linear mixed effect model was used to compare cell subcluster proportions, and changes were considered significant based on multiple comparisons adjusted *P* value (*P*.adj) < 0.05 for interaction between time and PFS group (i.e., the change from baseline to first response was different in the GMpfs and LMpfs groups) and an *P*.adj < 0.05 by Tukey *post hoc* testing (i.e., the change from baseline to first response was significant in at least one of the PFS groups). **C,** Box and dot plots of cell proportions for naïve B cells. Lines connect the dots corresponding to the same patient at each time point. *P* values were calculated using Tukey *post hoc* testing as described in (**A**). **D,** Bar plot of GSEA of naïve B cells (top) and memory B cells (bottom) comparing GMpfs with LMpfs. **E,** Dot plot displaying the relationship between naïve B abundance and diversity of Ig gene expression in post-BM B cells. Based on the enrichment for migration in naïve B cells and germinal center formation/isotype switching in memory B cells, we evaluated the diversity of Ig gene expression in these subclusters [i.e., the B subclusters that have typically left the BM]. R value and significance were calculated using Pearson correlation. **F** and **G,** Kaplan–Meier curve for the derivation (**B**) and validation (**C**) cohorts of PFS. HR (HazR) and *P* value calculated by Cox proportional hazards model. **H,** Line plot showing the Shannon index on serum Igs from ASCT to progression. For the 215 patients who experienced progression on the study, the day of ASCT was treated as day 0, and each visit between ASCT and disease progression was partitioned into buckets of 10% (e.g., 0%–10%, 10%–20% of the days from ASCT to progression) to visualize patients with different PFS on a comparable scale. [**A,** Created in BioRender. Ohlstrom, D. (2025) https://app.biorender.com/illustrations/69934a33256751e895217d78]

stratifying 20.5% of patients as Shannon-low (inferred to have less robust B-cell reconstitution) and 79.5% of patients as Shannon-high, consistent with 75% of patients increasing naïve B cells after ASCT (Fig. 3C). The low Shannon index samples were associated with shorter PFS in both the derivation [hazard ratio (HR) = 2.3; $P = 4.9e^{-5}$] and validation cohorts (HR = 2.1; $P = 2.3e^{-4}$; Fig. 3F and G). OS was also poorer for the low-Shannon group in the derivation cohort (HR = 2.2; $P = 5.2e^{-3}$) and did not reach significance in the validation cohort (HR = 1.5; $P = 0.13$; Supplementary Fig. S12B and S12C). To further characterize whether differences in outcomes were seen by the Shannon group while accounting for the ISS stage, we compared high- and low-Shannon groups within ISS stage I, II, and III patients, finding that PFS was generally worse in the low-Shannon group (Supplementary Fig. S12D–S12G). Finally, to determine how Ig diversity changed over time in patients with high/low Shannon index after ASCT, we evaluated the 215 patients who progressed during the study period (i.e., not censored). Treating the day of ASCT as day 0, we observed that patients with high post-ASCT Shannon index on serum Ig sustained high Shannon values until progression (Fig. 3H). Although the Ig diversity of patients with a low post-ASCT Shannon index increased over time, it did not reach comparable values to those of patients with a high post-ASCT Shannon index (Fig. 3H). Consistent with prior studies, this suggests that lack of Ig recovery within 1 year of ASCT may be associated with longer-term deficits in B-cell reconstitution, and naïve B cells may be a valuable subtype for identifying at-risk patients.

$CD16^+$ Monocytes Support B-cell Activity and Diverse Ig Production

To characterize the intercellular interactions that may contribute to diverse Ig production, we evaluated the expression of receptors/ligands in non-B cells that modulate B-cell function. First, to determine which cell types in the IME may indirectly influence diverse Ig production, we correlated the post-ASCT change (L_2FP) of each non-B immune cell type with Ig Shannon index. Interestingly, $CD16^+$ monocytes were the only cell type with a significant correlation with Ig diversity (R = 0.54, P.adj = 0.032) and have been previously reported to associate with B-cell differentiation and Ig production (27), suggesting a possible interaction with B cells that would contribute to diverse Ig production (Fig. 4A). To infer ligand/receptor interactions, we next performed cellular communication analysis using CellChat (22). Several interactions known to influence B-cell activation and differentiation were identified between $CD16^+$ monocytes and B subpopulations, including BAFF–BAFF-R (*TNFSF13B–TNFRSF13C*), CD45–CD22 (*PTPRC–CD22*), and MIF–CD74/CXCR4 (Fig. 4B–D; refs. 28, 29). Thus, the putative relationship between $CD16^+$ monocytes and diverse Ig production seems to be supported by plausible ligand/receptor interactions.

Next, to further depict the potential transcriptomic drivers of these interactions, we examined the differentially expressed genes in monocyte and B cells. Compared with the other clusters of monocytes that were not correlated with Ig diversity, $CD16^+$ monocytes had increased levels of *CD48* ($L_2FC = 0.76$, P.adj = $1.4e^{-33}$), a cell surface receptor that binds *SLAMF1*/CD244 to promote B-cell activation (30), as well as *BCL2A1* ($L_2FC = 0.72$, P.adj = 5.1^{-23}), which promotes monocyte survival in the IME (Fig. 4E and F; ref. 31). Consistent with the increased activation of B cells from the GMpfs group observed in GSEA (Fig. 3D) and the comparatively weaker CD45–CD22 interaction observed in cellular communication analysis (Fig. 4B and C), both naïve and memory B cells had decreased expression of the BCR antagonist, *CD22* (32), (naïve: $L_2FC = -0.41$, P.adj = $2.2e^{-10}$, memory: $L_2FC = -0.42$, P.adj = $2.6e^{-3}$, Fig. 4G). Concurrently, there was an increase in the downstream B-cell activation gene *NFKB2* (naïve: $L_2FC = 0.25$, P.adj = $1.6e^{-6}$, memory: $L_2FC = 0.47$, P.adj = $1e^{-4}$, Fig. 4G; ref. 33). These results indicate a potential supportive role for $CD16^+$ monocytes in fostering B-cell activation and Ig repertoire diversity following ASCT. Through the expression of costimulatory molecules, and in concert with heightened BCR signaling observed in GMpfs patients, these subsets may represent critical cell types/subtypes linking innate immune remodeling to humoral immunity.

Cancer–Testis Antigen Expression Multiple Myeloma Associates with B-cell Depletion at First Progression

To understand how myeloma dysregulates the IME at first progression, we compared the gene expression and genetic alterations of $CD138^{pos}$ bulk RNA-seq and whole-genome sequencing from 67 patients with matched baseline and first-progression biopsies, searching for genes strongly associated with this relapse event (Fig. 5A). Interestingly, differential expression of myeloma cells from first progression versus baseline depicted significantly increased expression of several cancer–testis antigen (CTAg), genes that are typically epigenetically silenced outside of the developing germ cells and placenta but exhibit pleiotropic functions in human cancers and are associated with elevated risk in multiple myeloma (Fig. 5B; refs. 34–36). Paradoxically, CTAgs are frequently expressed in myeloma cells and can elicit a natural antitumor immune response (35), suggesting that these cells leverage additional mechanisms to prevent IME control. Examining the expression of CTAgs, we observed significant sample-wise heterogeneity with a subset of samples ($n = 27$) driving the differential expression of CTAg genes (e.g., CTAG2: 35.8% of samples, SSX1: 32%, PAGE2B: 8.2%, and MAGEA3: 32.8%, Supplementary Fig. S13A and S13B). These 27 of the 134 samples were labeled CTAg-enriched; four came from baseline samples, out of which three had persistent enrichment to progression, and 20 samples were not enriched at baseline but became enriched at first progression (Supplementary Fig. S14A). This pattern of a gene expression profile that is rare at baseline with increased prevalence at progression was also observed for a group of patients with multiple myeloma with high expression of proliferation-related genes in a recent CoMMpass study by Skerget and colleagues (37). The proliferation-related genes enrichment analysis demonstrated that CTAg-enriched samples expressed significantly higher proliferation-associated genes and pathways ($P = 1.9e^{-8}$; Fig. 5C; Supplementary Fig. S14B). These findings do not seem to be confounded by clinical covariates as the CTAg-enriched and "other" cohorts had similar distributions of age ($P = 0.17$),

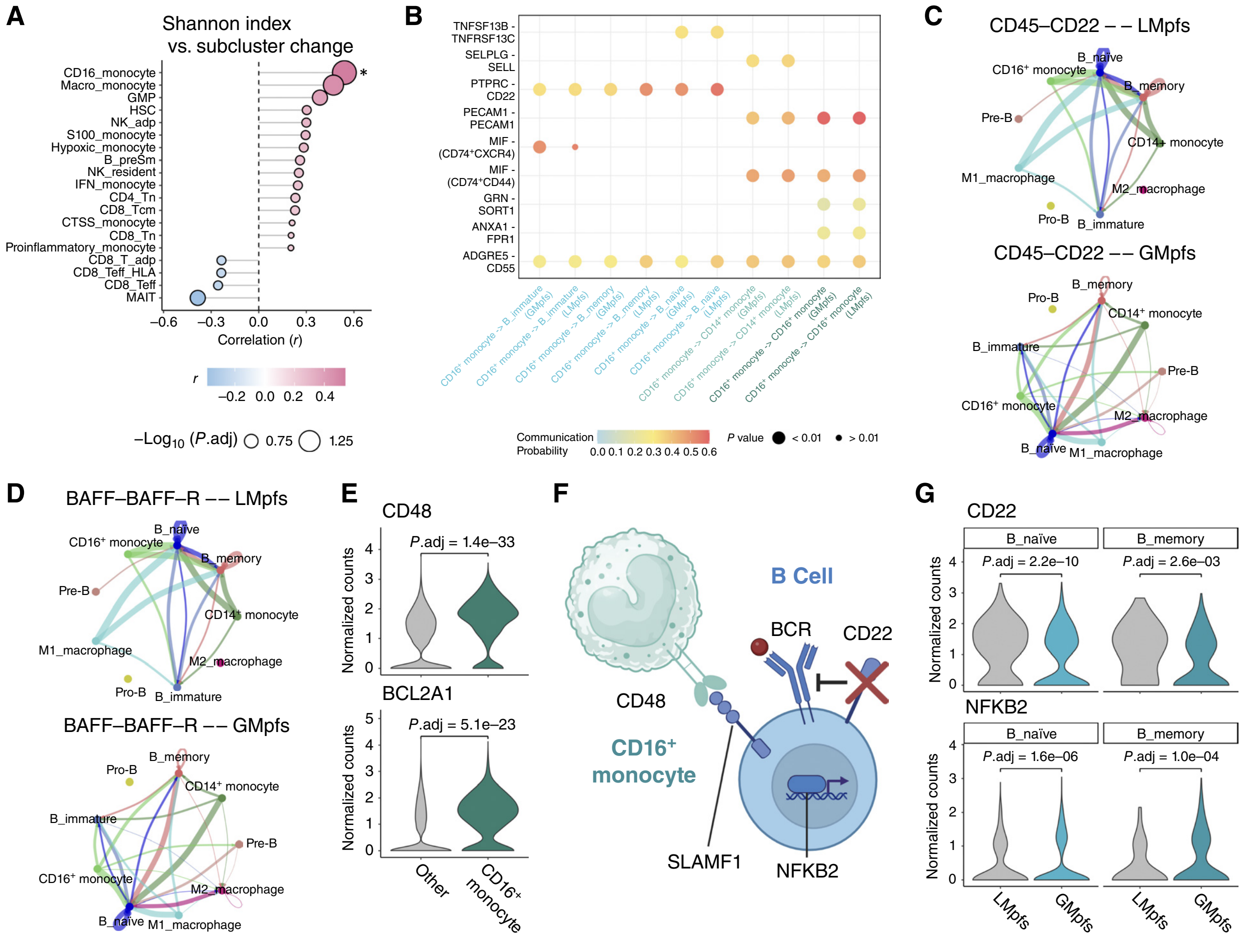

Figure 4. CD16⁺ monocytes support B-cell activity and diverse Ig production. **A,** Lollipop plot for correlation of non-B subclusters abundance with Ig diversity. To identify non-B subclusters that associated with high Ig diversity, we correlated each other subcluster's $\log_2$ fold proportion with the same Shannon index values calculated in (**E**). R value and significance were calculated using Pearson correlation with an asterisk denoting $P < 0.05$. **B,** Dot plot of pathways with differential communication probability between the GMpfs and LMpfs groups. **C** and **D,** Chord plots displaying predicted CD45–CD22 (**C**) and BAFF–BAFF-R (**D**) interaction strength. Width of the arrows between two subclusters indicates relative interaction strength predicted by CellChat. **E,** Violin plots of normalized counts of *CD48* (top) and *BCL2A1* (bottom) in CD16⁺ monocytes and all other monocytes in first-response post-ASCT samples. Benjamini–Hochberg adjusted *P* values were calculated in limma. **F,** Schematic representation of possible interaction between CD16⁺ monocytes and B cells. **G,** Violin plots of normalized counts of *CD22* (top) and *NFKB2* (bottom) in naïve and memory B cells comparing LMpfs with GMpfs patients in first-response post-ASCT samples. Multiple comparisons adjusted *P* values were calculated using limma. [**F,** Created in BioRender. Ohlstrom, D. (2025) https://app.biorender.com/illustrations/69934b9e230d7098b7cb46c9]

baseline ISS stage ($P = 0.58$), induction therapy ($P = 0.64$), and ASCT ($P = 1$; Supplementary Fig. S15A–S15D). Also consistent with Skerget and colleagues (37), we found that patients with CTAg enrichment at first progression had considerably shorter time to second progression (HR = 2.9; $P = 1.5e^{-3}$) and OS (HR = 4.5; $P = 5.8e^{-6}$; Supplementary Fig. S16A–S16D). In addition to expressing higher levels of CTAgs, this subgroup of samples also expressed more unique CTAg genes, with a median of 21 CTAgs >1 transcript per million (TPM) as compared with two CTAgs >1 TPM from all other samples, suggesting epigenetic dysregulation of CTAg in multiple myeloma reversing normal silencing to enhance protumoral properties ($P = 4.9e^{-5}$; Fig. 5C). Supporting this hypothesis, we found that CTAg enrichment was not associated with common multiple myeloma–driving copy number alterations (CNA), single-nucleotide variants (SNV), structural variants (SV), or fusion transcripts (Supplementary Fig. S17A and S17B) but rather had preferential alteration in genes that code for chromatin modifying proteins (Supplementary Figs. S17C–S17E, S18A, and S18B). Finally, CTAg-enriched samples highly expressed several genes encoding cytokines and chemokines, including IL32, FAM3B, and CXCL8 ($P = 5.7e^{-10}$; Fig. 5C). Thus, it seems that CTAg-enriched multiple myeloma leverages both proliferative signaling and inflammatory cytokine expression to subvert the immunologic constraints of the IME at disease progression. These findings suggest a distinct transcriptional program characterized by CTAg enrichment, proliferation, and immune modulation that may enable immune dysregulation and disease acceleration.

CTAg-Enriched Myeloma Associates with B-cell Depletion

Given that CTAg multiple myeloma highly expressed several cytokines and chemokines, we hypothesized that these patients would exhibit alterations in their IME composition.

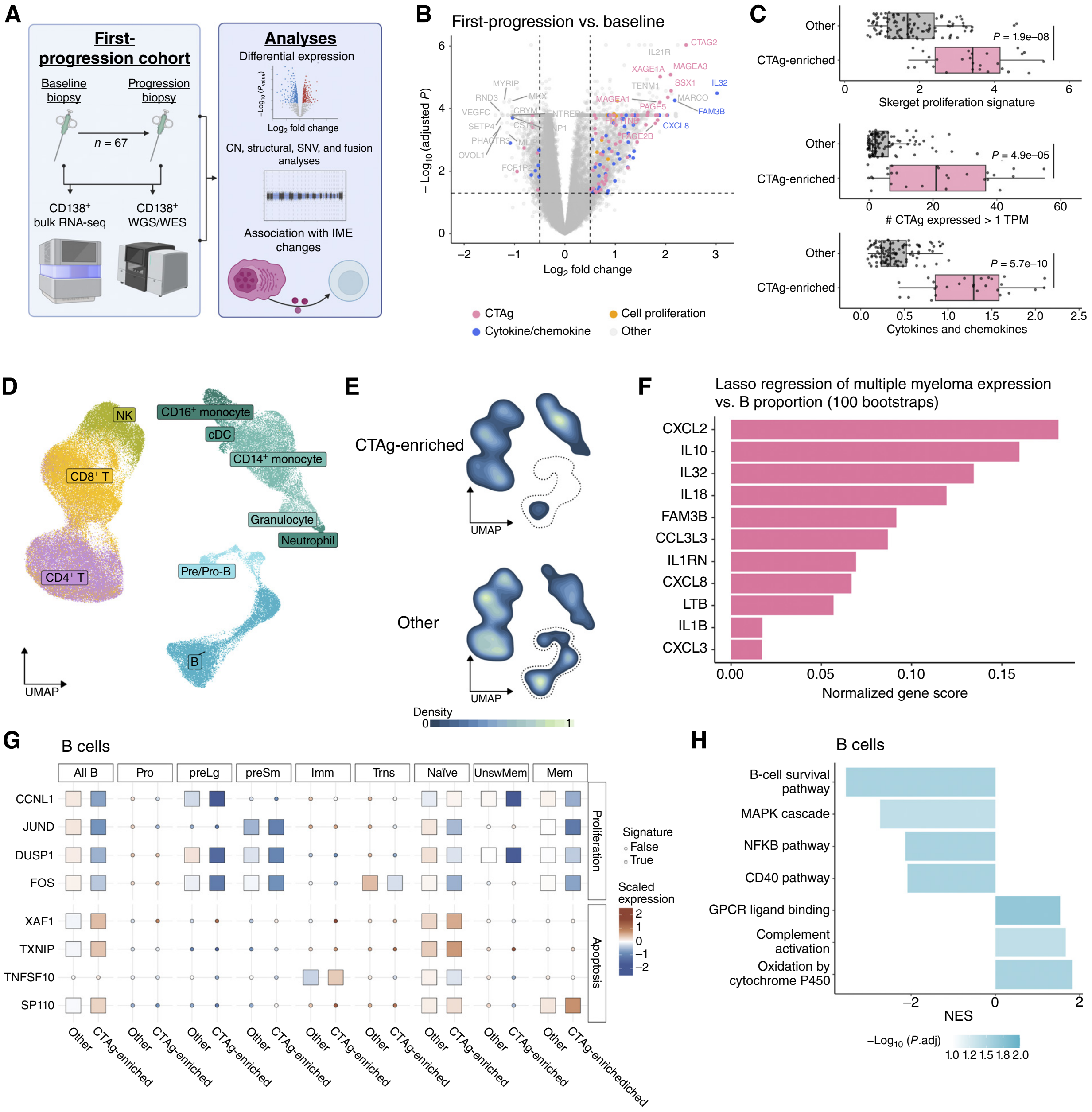

Figure 5. CTAg expression multiple myeloma associates with B-cell depletion at first progression. **A,** Schematic for the longitudinal analysis of CD138^{pos} bulk RNA-seq and whole-genome sequencing ($n = 67$). **B,** Volcano plot displaying the differentially expressed genes comparing baseline vs. first progression. Differential expression was executed using limma–voom with significance cut point of absolute $\log_2$ fold change >0.5 and multiple comparisons adjusted P value < 0.05. **C,** Box plots of proliferation gene signature published in Skerget and colleagues (37), number of CTAgs with >1 TPM, and enrichment for cytokine/chemokine DEGs. P value calculated by Student t test. **D** and **E,** UMAP embeddings for lymphoid cells in CD138^{neg} scRNA-seq of samples from first progression and corresponding density plots displaying the normalized density of cells. **F,** Bar chart displaying the cytokine/chemokine genes expressed in multiple myeloma associated with naïve B depletion. One-hundred bootstrapped iterations of Lasso regression were performed with cytokine/chemokine gene expression (CD138^{pos} bulk RNA-seq) as the candidate predictors of proportion of naïve B cells (CD138^{neg} scRNA-seq). Feature importance scores were calculated by the normalized, average r value weighted by the proportion of iterations in which the feature was included in the Lasso model. **G,** Heatmap displaying the patient-wise scaled expression of pro-proliferation and proapoptotic genes in B cells from first-progression samples. Significance was calculated using limma–voom with Benjamini–Hochberg multiple comparison correction. **H,** Bar plot of GSEA of B cells comparing CTAg-enriched samples with all other samples. UMAP, Uniform manifold approximation and projection; WES, whole exome sequencing; WGS, whole genome sequencing. [**A,** Created in BioRender. Ohlstrom, D. (2025) https://app.biorender.com/illustrations/69934c4aea7cfb7f41f28245]

Fifty-one patients had scRNA-seq of CD138^{neg} samples at first progression, with eight having CTAg-enriched multiple myeloma in their CD138^{pos} bulk RNA-seq. Strikingly, CTAg-enriched samples had significantly lower proportions of most B-cell lineages, including large pre-B ($L_2FP = -2.7$, $P.adj = 0.028$), small pre-B ($L_2FP = -2.6$, $P.adj = 4.7e^{-3}$), immature B ($L_2FP = -2.8$, $P.adj = 1e^{-3}$), naïve B ($L_2FP = -1.5$, $P.adj = 0.028$), transitional B ($L_2FP = -3.1$, $P.adj = 1e^{-3}$), and memory

B ($L_2FP = -2.8$, P.adj = 0.014, Fig. 5D and E; Supplementary Fig. S19A–S19I). This finding was particularly notable given that naïve B cells were previously found to be at higher proportion after ASCT in patients with sustained response (Fig. 3B). Furthermore, the percentage of plasma cells in the BM at relapse was comparable between patients with CTAg-enriched multiple myeloma and others ($P = 0.095$; Supplementary Fig. S20), suggesting that it was not plasma cell load but another mechanism such as intercellular signaling that influenced the IME composition. To identify which genes expressed in CTAg-enriched multiple myeloma associate with B-cell depletion, we performed Lasso regression of cytokine/chemokine expression in multiple myeloma cells with B-cell proportion. Six genes explained most of the variation in naïve B proportion: *CXCL2*, *IL10*, *IL32*, *IL18*, *FAM3B*, and *CCL3L3* (Fig. 5F; Supplementary Fig. S21A and S21B). Of these, IL10 (38) and IL32 (39) are known to suppress B cells. Concurrently, B cells in CTAg-enriched samples had increased expression of proapoptotic genes (*XAF1*: $L_2FC = 0.44$, P.adj = $1.3e^{-46}$, *TXNIP*: $L_2FC = 0.33$, P.adj = $3.4e^{-9}$, *SP110*: $L_2FC = 0.27$, P.adj = $4.9e^{-13}$) and decreased expression of pro-proliferative genes (*JUND*: $L_2FC = -0.85$, P.adj = $1.1e^{-98}$, *FOS*: $L_2FC = -0.65$, P.adj = $6.1e^{-42}$, *CCNL1*: $L_2FC = -0.51$, P.adj = $3.2e^{-39}$, *DUSP1*: $L_2FC = -0.40$, P.adj = $2.7e^{-26}$, Fig. 5G). Of the B-cell subclusters, naïve cells seem to be particularly suppressed with both decreased expression of proliferative genes and increased expression of proapoptotic genes (Fig. 5G). Consistent with these findings, GSEA identified significantly decreased enrichment for the B-cell survival pathway in B cells from CTAg-enriched samples (NES = −3.5, P.adj = 0.028) as well as B-cell activation pathways such as NFKB (NES = −2.1, P.adj = 0.028, Fig. 5H). These data suggest that CTAg-enriched multiple myeloma may promote a cytokine/chemokine-driven reshaping of the IME that may suppress B-cell development through direct and indirect mechanisms to support IME dysregulation. CTAg-enriched multiple myeloma is associated with low levels of B-cell populations, particularly naïve B cells, potentially driven by elevated cytokines such as *IL10* and *IL32*. Together, these findings associate CTAg expression with impaired B-cell development. However, several of the genes identified by Lasso regression are known to act on other cells in the IME, so we next aimed to characterize how myeloid and $CD8^+$ T cells are altered in CTAg-enriched samples.

CTAg-Expressing Multiple Myeloma Supports MSDC and T-cell Exhaustion–Associated Gene Expression

The cytokines and chemokines overexpressed in $CD138^{pos}$ bulk RNA-seq of CTAg multiple myeloma include known myeloid-attracting chemokines *CXCL2* and *CCL3* (40), as well the lMDSC-promoting cytokine, *IL18* (41), prompting us to evaluate the myeloid compartment as a potential indirect mechanism by which CTAg multiple myeloma creates a suppressive IME. Differential expression of monocytes from CTAg-enriched samples to all other samples found hallmarks of MDSC gene expression, including increased leukocyte Ig-like receptor (LILR) genes (e.g., *LILRB4*: $L_2FC = 0.34$, P.adj = $3.7e^{-199}$, *LILRB1*: $L_2FC = 0.40$, P.adj = $4.3e^{-104}$) and decreased MHC-II (e.g., *HLA-DRB1*: $L_2FC = -0.51$, P.adj = $2.8e^{-99}$, *HLA-DRA* $L_2FC = 0.30$, P.adj = $2.8e^{-28}$, Fig. 6A and B). Calculation of a monocytic MDSC gene expression enrichment score using a previously published gene signature (42) found enrichment in monocytes from CTAg-enriched samples relative to other samples ($P = 1.9e^{-156}$; Fig. 6C). Supporting the possible indirect role of monocytes in suppressing the IME in CTAg samples, GSEA identified significant enrichment immunosuppressive pathways, including FCGR3A-mediated IL10 synthesis (NES = 2.3, P.adj = $3.7e^{-3}$) as well as decreased antigen presentation (NES = −3.6, P.adj = $4.5e^{-3}$, Fig. 6D). These findings suggest that CTAg-expressing multiple myeloma reshapes the IME by promoting MDSC-like features in monocytes, thereby fostering a suppressed immune niche that may contribute to disease progression.

Finally, to determine whether the $CD8^+$ T compartment is influenced by the presence of CTAg multiple myeloma, we examined the gene expression in CTAg-enriched samples (Fig. 6E). Interestingly, $CD8^+$ T cells had increased expression of cytotoxic genes, including *PRF1* ($L_2FC = 0.38$, P.adj = $6.6e^{-69}$), *GZMA* ($L_2FC = 0.49$, P.adj = $4.3e^{-64}$), and *GZMK* ($L_2FC = 0.50$, P.adj = $1.3e^{-65}$, Fig. 6F and G). The cytotoxic enrichment observed seems to be an indication of prolonged stimulation, as $CD8^+$ T cells from CTAg-enriched samples depicted significantly higher markers chronic inflammation (*CCL4*: $L_2FC = 0.26$, P.adj = $1.2e^{-18}$, *LY6E*: $L_2FC = 0.37$, P.adj = $8e^{-89}$) and markers of exhaustion, including *LAG3*, ($L_2FC = 0.32$, P.adj = $2.8e^{-161}$), *HAVCR2* ($L_2FC = 0.28$, P.adj = $1.9e^{-250}$), *CTLA4* ($L_2FC = 0.28$, P.adj = $1e^{-250}$), *PDCD1* ($L_2FC = 0.27$, P.adj = $1e^{-250}$), and *TIGIT* ($L_2FC = 0.25$, P.adj = $5.3e^{-88}$, Fig. 6F). This is further supported by the finding that the effector and effector memory populations had the greatest frequency of increased expression of exhaustion markers, potentially implying that an ineffective cytotoxic response in the context of an immunosuppressive IME lead to $CD8^+$ T-cell exhaustion. GSEA similarly identified decreased activity of canonical T-cell activation pathways such as TCR signaling (NES = −4.8, P.adj = 0.021), RUNX3 activity (NES = −5.3, P.adj = $4.6e^{-3}$), and TNF signaling (NES = −4.7, P.adj = $4.8e^{-3}$, Fig. 6H). Together, these data suggest that CTAg-enriched multiple myeloma promotes immune dysfunction—associating with depleted B cells, MDSC-like phenotype in monocytes, and expression of exhaustion markers in $CD8^+$ T cells—potentially limiting immune-mediated disease control at relapse. These insights highlight CTAg expression as a biomarker of immune resistance and suggest that targeting CTAg-associated immunosuppressive pathways may offer new therapeutic strategies to improve antitumor immunity in relapsed multiple myeloma.

Patients with 3+ Longitudinal Samples Depict Progressive Enrichment of CTAg Gene Expression

To evaluate how multiple myeloma genetics and transcriptomics progress through the disease course, we analyzed 13 patients with three or more matched $CD138^{pos}$ bulk RNA-seq and whole-genome sequencing samples (Fig. 7A). Six of the 13 patients had consistent increases in the number of CTAg genes expressed (>1 TPM) across longitudinal samples (Fig. 7B). All six patients received a PI and steroid as a part of their induction chemotherapy regimen, with four also receiving an IMiD and two receiving a DNA alkylator (Fig. 7C; Supplementary

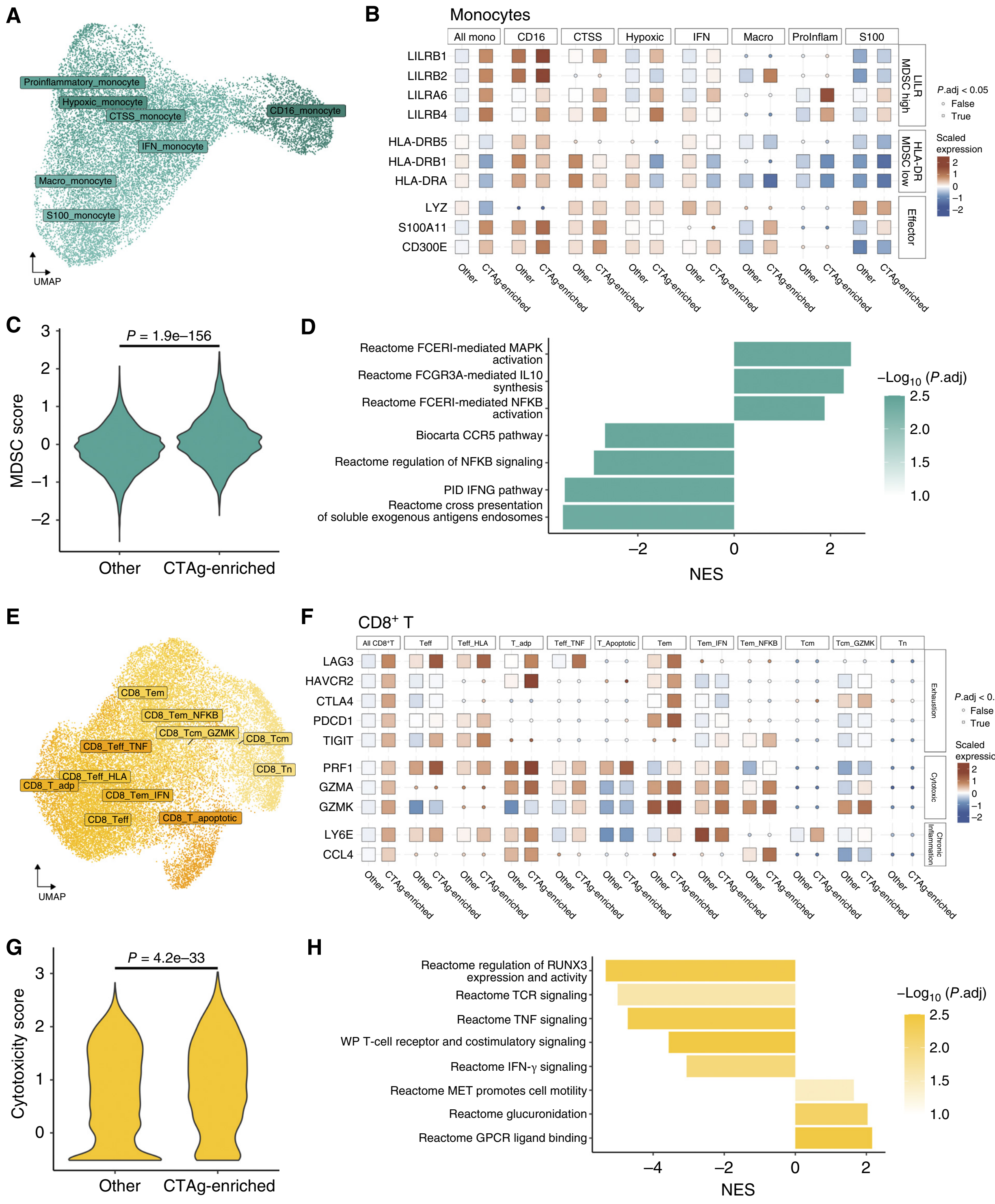

Figure 6. CTAg expressing myeloma supports MDSC and T-cell exhaustion. **A,** UMAP embeddings for myeloid cells in CD138^{neg} scRNA-seq of samples from first progression. **B,** Heatmap displaying the patient-wise scaled expression of MDSC-related genes in myeloid cells from first progression samples. Significance was calculated using limma–voom with Benjamini–Hochberg multiple comparison correction. **C,** Violin plot displaying MDSC score for myeloid cells from CTAg-enriched samples and all other samples. MDSC score calculated by the average of normalized scaled expression values for published MDSC markers. *P* value was computed using *t* test. **D,** Bar plot of GSEA of myeloid cells comparing CTAg-enriched samples with all other samples. **E,** UMAP embeddings for CD8$^+$ T cells in CD138^{neg} scRNA-seq of samples from first progression. **F,** Heatmap displaying the patient-wise scaled expression of exhaustion and chronic inflammation–related genes in CD8$^+$ T cells from first-progression samples. Significance was calculated using limma–voom with Benjamini–Hochberg multiple comparison correction. **G,** Violin plot displaying cytotoxicity score for CD8$^+$ T cells from CTAg-enriched samples and all other samples. Cytotoxicity score calculated by the average of normalized scaled expression values for published cytotoxicity markers. **H,** Bar plot of GSEA of CD8$^+$ T cells comparing CTAg-enriched samples with all other samples. UMAP, Uniform Manifold Approximation and Projection.

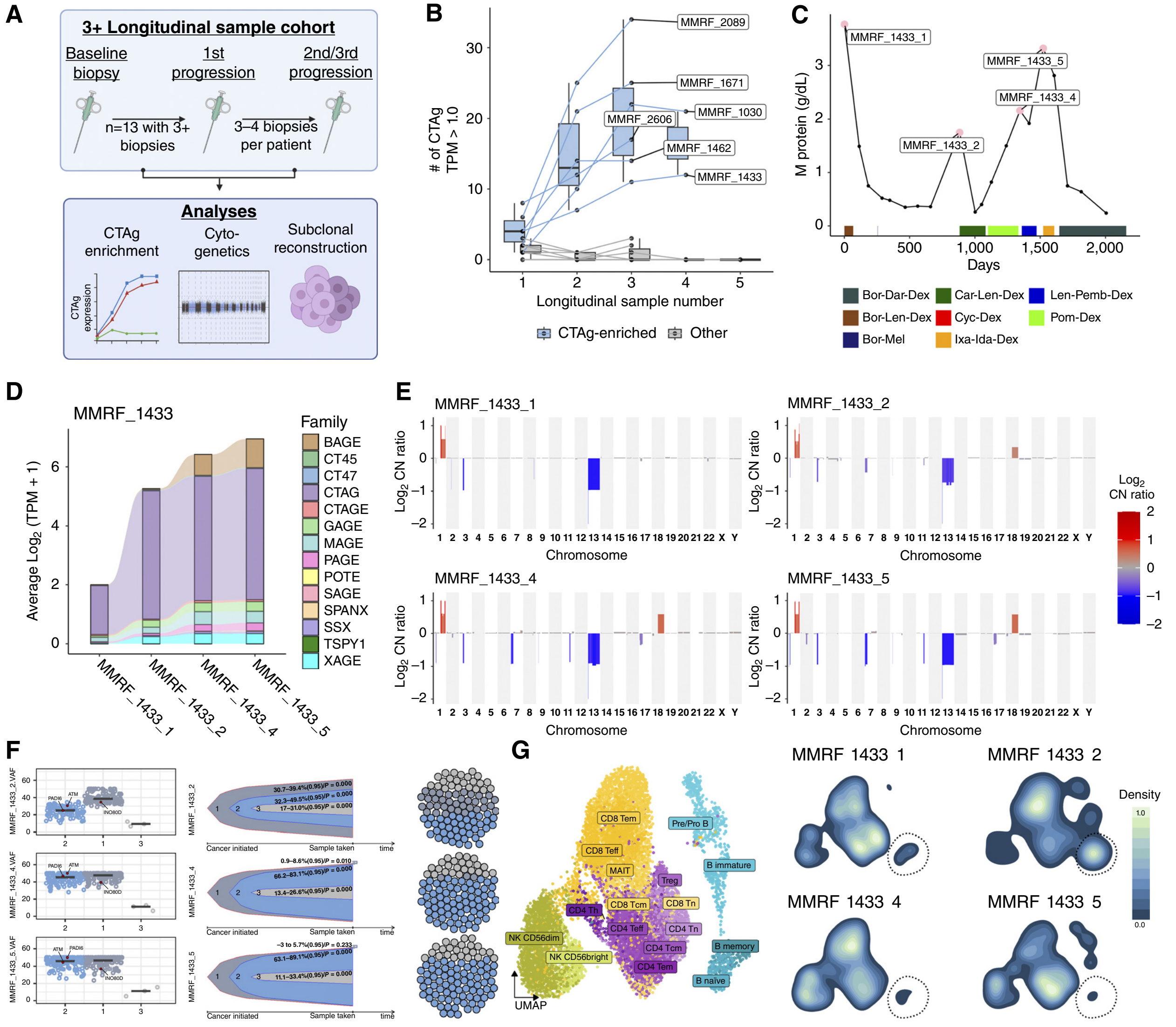

Figure 7. Longitudinal evaluation of patients with three or more samples in CD138^{pos} DNA and RNA sequencing. **A,** Schematic representation of longitudinal analysis of 13 patients with three or more samples. **B,** Box and line plot displaying the number of CTAg genes expressed at > 1 TPM in CD138^{pos} bulk RNA-seq. Six of 13 samples had progressive increases in CTAg expression (blue), whereas seven patients had three or fewer CTAgs expressed across longitudinal samples (gray). **C,** Line plot of serum M protein measurements over time. Pink dots and labels annotate the visits at which biopsies were taken for RNA and DNA sequencing. Patient 1433 is presented as a representative example, with corresponding data for the other five patients shown in Supplementary Figs. S22–S26. **D,** Alluvial plot of CTAg gene expression across longitudinal samples. **E,** Copy number plot split by longitudinal samples. **F,** Subclonal reconstruction of longitudinal samples. Subclonal structure was inferred based on the cancer cell fraction of SNVs using QuantumClone. SNVs in genes coding for chromatin modifying proteins are labeled and highlighted in red (left). Bell plots display inferred subclonal evolution from the SNV cancer cell fractions (middle). Dot chart depicts the relative proportion of each subclone across time points (right). **G,** UMAP embeddings for lymphoid cells and corresponding density plots displaying the normalized density of cells. CN, copy number; UMAP, Uniform manifold approximation and projection. [**A,** Created in BioRender. Ohlstrom, D. (2025) https://app.biorender.com/illustrations/69934ca34d35e742fa947724]

Figs. S22–S26A). Despite therapy, all six patients exhibited not only increased in expression of CTAg genes (log$_2$ TPM) but also acquired expression of a greater number of CTAg families across progressions, suggesting increasing (epi)genetic dysregulation over time (Fig. 7D; Supplementary Figs. S22–S26B). Consistent with the longitudinal two-sample analysis (Fig. 5), there were not unifying cytogenetic changes across samples, with three patients having odd-number-trisomes, four 1q gain, and three with chr13 deletion (Fig. 7E; Supplementary Figs. S22–S26C). Whereas many of these lesions are associated with poor outcomes, none were consistently observed across CTAg-expressing samples, suggesting that CTAg upregulation during disease progression is not driven by a shared cytogenetic mechanism. Instead, these data point toward an alternative driver—potentially epigenetic in nature—underlying the stepwise accumulation of CTAg expression across samples.

To determine whether CTAg-expressing multiple myeloma cells exhibited increased chromatin-modifying mutations, we performed subclonal reconstruction on the SNVs detected across time points. Consistent with our longitudinal two-sample analysis, four of the samples depicted persistent or increasing clonality of nonsynonymous mutations in chromatin-modifying genes, including *TRRAP* (43), a histone acetyltransferase, *KDM3B* (44), a demethylase, *INO80D* (45), a member of the INO80 chromatin remodeling complex, *PADI6*, a peptidyl arginine deiminase that has been shown to influence transcriptional state via H4 acetylation (46), as well as genes involved in general DNA stability, including *ATM* and *TP53* (Fig. 7F; Supplementary Figs. S22–S26D; ref. 47). Interestingly, patient 1433 did not have mutations detected in *INO80D* or *PADI6* at baseline when CTAg expression was relatively low and then at first progression had clonal *INO80D* mutation and subclonal mutation of *PADI6* and *ATM*, with all three being clonal in subsequent samples (Fig. 7F). These changes correlated with the progressive increase in CTAg expression, potentially indicating connection between the two. Patient 1433 also had CD138^{neg} scRNA-seq at the same four time points. Examining their corresponding IME profile through their disease course, their first progression had naïve B cells comprising 11.7% of the IME (Fig. 7G). However, after a brief response (Fig. 7C), patient 1,143 had a second progression after which they had persistently low naïve B-cell percents (third sample: 1.8%, fourth sample: 0.9%). Taken together, these longitudinal analyses suggest that CTAg expression may be shaped by the clonal evolution of mutations in chromatin-modifying genes and that such transcriptional reprogramming may be linked to IME remodeling. In particular, the case of patient 1433 illustrates a potential trajectory in which acquisition and increased clonality of chromatin regulatory mutations coincides with both increasing CTAg expression and declining naïve B-cell abundance, reinforcing the proposed connection between epigenetic dysregulation and immune dysregulation in relapsed multiple myeloma.

DISCUSSION

In this study, we longitudinally evaluate the dynamics of myeloma and its IME across baseline at diagnosis, response to therapy, and disease progression. By utilizing CD138^{neg} scRNA-seq, CD138^{pos} bulk RNA-seq, and whole-genome sequencing, we provided a deep mechanistic exploration of multiple myeloma biology in the BM. Our analyses build on previous studies to provide a detailed characterization of how interactions between the B lymphoid, T lymphoid, and myeloid compartments shape the IME after induction with and without ASCT (7–9). Evaluation of outcomes in patients with CD138^{neg} scRNA-seq identified IME correlates of sustained response after ASCT. Finally, evaluation of myeloma profiles and the IME at first (and subsequent) progression identified CTAg enrichment as associated with development of malignant disease features and immune suppression. This integrative, multi-omic approach not only advances our understanding of the evolving immune landscape in multiple myeloma but also establishes a framework for identifying actionable biomarkers and therapeutic targets, paving the way for more personalized and effective treatment strategies.

By evaluating the composition of the IME in matched samples at diagnosis and first response after induction or after induction and ASCT, we uncovered transcriptional changes and putative intercellular signaling interactions that hinder memory phenotype during the post-ASCT reconstitution period. Consistent with previous studies (9–11), we observed that post-ASCT samples had a proportional increase in early B-cell subclusters as well as a proportional decrease in naïve, central memory, and helper T cells. In the CD8$^+$ T compartment, effector and early apoptotic cells expanded after ASCT, whereas effector memory cells were depleted, suggesting a skew in the effector cells that develop immunologic memory. This imbalance potentially contributes to suboptimal immune function during the reconstitution period and may benefit from balancing the cell fate outcomes. Whereas the observed skew likely represents CD8$^+$ T-cell dysfunction, it does not resolve the impact on T-cell clonality; future CoMMpass studies utilizing 5′ scRNA-seq will examine how induction therapy influences the degree to which CD8$^+$ T cells exhibit clonal versus bystander expansion. Cell communication, TF enrichment, and GSEA depicted TNF and type II IFN signaling between CD16$^+$ monocytes and CD8$^+$ T cells, both of which promote highly inflammatory IME and may support the observed bias in CD8$^+$ effector T cells (23). Historically administration of type II IFN shortly after ASCT has not improved outcomes in multiple myeloma and other hematologic malignancies (48), though the timing of administration may be an important variable influencing the impact of IFN on immune reconstitution. We hypothesize that therapeutically inhibiting these signaling pathways has the potential to improve the balance of effector memory formation and promote productive tumor surveillance, potentially increasing the duration of response after ASCT.

The IME is critical for regulating multiple myeloma, with previous studies identifying B-cell repopulation as a positive prognostic biomarker and exhausted T cells as a poor prognostic biomarker (9, 10). Building on these works, we found that naïve B cells seem to be a critical subcluster supporting sustained response. Given that naïve B cells typically have departed from the BM and undergone further development in a secondary lymphoid organ, their presence as higher proportion in a BM biopsy suggests a larger pool of mobile naïve B lymphocytes in the circulation to undergo maturation. This was reflected in the enrichment for migratory pathways in naïve B cells from patients with greater than median PFS as compared with those with less than median PFS. We additionally found that the proportional abundance of naïve B cells associated with downstream enrichment for isotype switching and germinal center formation in memory B cells, indicating a more robust B-cell immune reconstitution. Whereas our analyses utilized binary stratification by median PFS, future studies utilizing survival models considering IME composition and other clinical covariates from a larger cohort of patients will be valuable to validate our findings. Furthermore, we found that the differences in Ig diversity were also detectable in the serum of the 408 patients in the CoMMpass clinical serum Ig measurements. Consistent with our scRNA-seq analysis, we found that high Ig diversity was associated with sustained response in our equally split derivation and validation cohorts from the CoMMpass dataset. This builds on existing studies that described the improved prognosis of patients with Ig recovery after ASCT (49, 50). Our findings suggest that increased Ig diversity and interactions between specific B-cell subsets and other cells in the IME (e.g., myeloid cells) contribute to sustained response after ASCT, though dedicated studies are needed to directly compare post-ASCT Ig metrics to determine which are most predictive of patient outcomes while accounting for variables such as baseline risk and depth of treatment response. These findings suggest that post-ASCT immune composition plays a critical role in patient outcomes.

Longitudinal evaluation of the CD138^{pos} compartment further enabled us to uncover potential expression patterns utilized by multiple myeloma to circumvent the IME at disease progression. Differential expression of longitudinal baseline and first progression samples identified enrichment for CTAgs, proliferation, and cytokine/chemokine expression. Consistent with recent work by Skerget and colleagues (37), we found that this pattern of gene expression associated with inferior outcomes and was rare at baseline (4 of 67 patients) but became much more common at first progression (23 of 67 patients). Importantly, this gene expression pattern did not correlate with common multiple myeloma cytogenetic alterations, SVs, SNVs, or fusion events but was instead enriched in cases harboring mutations in chromatin-modifying genes. Building on existing studies implicating CTAgs as a high-risk feature of multiple myeloma (35, 36), we found that patients with CTAg-enriched multiple myeloma exhibited profound IME alterations, including B-cell depletion, increased MDSC-like phenotype in monocytes, and increased expression of exhaustion markers in T cells. The presence of T-cell exhaustion has also been recently observed in extramedullary multiple myeloma (51, 52) and BM breakout lesions (53), suggesting a potentially conserved immune signature of multiple myeloma that associates with poor outcomes. In contrast to focal multiple myeloma sites, as well as solid tumors (54), markers of exhaustion were observed throughout the CD8^{+} T-cell compartment and did not form a discrete cluster. Further studies are warranted to tease out the conserved and discrepant features of T-cell exhaustion across multiple myeloma sites and cancer types. In multiple myeloma, these features of immune dysfunction do not seem to be driven solely by disease burden, given the similar multiple myeloma cell percentages between CTAg-enriched and other samples, though the lack of detected differences may be due to the sensitivity limitations of flow cytometry. Instead, CTAg-enriched tumors expressed high levels of immunosuppressive cytokines such as IL10, suggesting potential therapeutic avenues to counteract CTAg-driven immune suppression. Longitudinal tracking in seven patients with 3 to 4 sequential samples demonstrated progressive increases in both CTAg expression and the cancer cell fraction of chromatin modifier mutations over time, supporting a role for CTAgs in clonal evolution and immune dysregulation. These findings extend previous works such as by Rasche and colleagues (55), illustrating that subclones of variable size early in the multiple myeloma disease course can become enriched over disease progression(s). However, the emergence of mutations in genes that code for chromatin modifiers co-occurs with mutations in many other genes. Although the correlation of aberrant expression of genes that are typically epigenetically repressed (CTAgs) and clonal expansion of mutations in chromatin modifiers is intriguing, further studies utilizing deep whole-genome sequencing of longitudinal samples from a large cohort of patients with multiple myeloma is needed to resolve relapse-driving mutations from bystander mutations. Together, these findings highlight CTAg-enriched multiple myeloma as a distinct and aggressive disease phenotype driven by epigenetic dysregulation and immune dysregulation—an entity not captured by current risk stratification schemes and one that may warrant targeted immunotherapeutic intervention, such as immunization approaches and tailored monitoring strategies (37, 56, 57).

Although this study provides novel insights into the dynamics of multiple myeloma and its IME following initial diagnosis and treatment, limitations exist, and additional follow-up studies are warranted to extend the findings of this project. First, the majority of samples in this study were collected at disease baseline, first response, and first progression, with a limited number of patients having more than two samples. Therefore, additional studies utilizing longitudinal samples at baseline, response after induction, response after ASCT, and progression, as well as at second/third responses/progressions, has the potential to enhance our understanding of how multiple myeloma–IME interactions become increasingly perturbed over time. Concurrently, our findings are limited by the lack of data regarding timing of stem cell collection, stem cell dose, and post-ASCT therapy. Future studies should account for, and ideally homogenize, these covariates to ensure bias is not introduced into the evaluation of IME reconstitution. Third, although the CoMMpass project offers a large sample size, multi-omic data, and mature clinical outcomes, it under-represents patients treated with newer therapies such as anti-CD38 antibodies (daratumumab) and chimeric antigen receptor T cells, especially in the frontline setting. Longitudinal studies of patients receiving these agents will be critical to characterize shared and distinct IME dynamics compared with those treated with induction regimens primarily using PIs, IMiDs, and steroids. Fourth, CTAgs are pleiotropic, and their functional consequences can be context-dependent (58). Detailed studies to isolate the relative contribution of CTAgs to multiple myeloma proliferation, IME alteration, and other disease features will provide a deeper understanding of how they contribute disease persistence. Finally, whereas CTAg expression is highly suggestive of chromatin dysregulation, we did not directly assay the chromatin state of CTAg-enriched multiple myeloma. Follow up studies will characterize the chromatin state of CTAg-enriched multiple myeloma to determine the exact mechanisms by which progressive CTAg expression is developed.

Our longitudinal analysis of one of the largest cohorts of matching CD138^{neg} scRNA-seq, CD138^{pos} bulk RNA-seq, and whole-genome sequencing adds to the valuable insights produced by the MMRF CoMMpass study. Naïve B repopulation and interaction with CD16^{+} monocytes are intriguing contributors to post-ASCT immune reconstitution CTAg enrichment, predominantly seen at disease progression, which seems to promote multi-faceted IME dysfunction. Ongoing studies will build on these findings to further define how these features influence patient outcomes, providing critical insights to design targeted therapeutics to enhance response to therapy.

METHODS

Ethics Approval and Participant Consent

All samples used in this study were obtained from the MMRF CoMMpass clinical trial (NCT01454297). All procedures involving human participants adhered to the ethical standards set by the MMRF research committee. Written informed consent was obtained from all participants for the collection and analysis of biospecimens and clinical data. The study protocol was approved by the Institutional Review Board at each participating medical center. A complete list of participating institutions is available at ClinicalTrials.gov (NCT01454297).

Sample Collection

A total of 243 CD138^{neg} BM mononuclear cell samples were collected from 102 patients with multiple myeloma enrolled in the MMRF CoMMpass study (NCT01454297), representing the patients with two or more samples in the Immune Atlas project (bioRxiv 2024.05.15.593193v1). Patients were monitored with quarterly follow-ups for up to 8 years following their initial diagnosis. Eligibility criteria included suitability for either standard triplet therapy (an IMiD, PI, and glucocorticoid) or doublet therapy, with the majority receiving triplet therapy as first-line treatment. Samples were collected at both pretherapy (baseline) and posttherapy (response or progression) time points and processed at four institutions: Emory University, Mayo Clinic Rochester, Mount Sinai School of Medicine, and Washington University.

CD138^{neg} Cell Isolation and Cryopreservation of Cell Samples

BM aspirates obtained from the Multiple Myeloma Research Consortium tissue bank were fractionated into CD138^{pos} (myeloma cells) and CD138^{neg} (immune and other BM cells) populations using immunomagnetic cell selection targeting CD138 surface expression (automated RoboSep and manual EasySep systems, StemCell Technologies, Inc.). Prior to bead-based separation, each sample was assessed for malignant plasma cell content using flow cytometry. CD138^{neg} cells were subsequently centrifuged at 400 × *g* for 5 minutes, and the resulting pellet was resuspended in freezing medium (90% fetal calf serum and 10% dimethyl sulfoxide) at a concentration of 5 to 30 million cells per mL. Samples were aliquoted, documented for cell concentration and storage location, and preserved in liquid nitrogen for future analysis.

scRNA-seq Sample Preparation, Library Construction, and Sequencing

To ensure high-quality and consistent single-cell data across sites, we developed a detailed 3′ scRNA-seq protocol using the 10x Genomics Chromium platform. Aliquots of CD138^{neg} BMME samples were thawed in a 37°C water bath, washed with warm medium, and pelleted by centrifugation at 370 × *g* for 5 minutes at 4°C. Cell pellets were resuspended in ice-cold phosphate-buffered saline (PBS) with 1% bovine serum albumin (BSA), and viability was assessed. Samples with viability below 90% underwent dead cell removal using the Dead Cell Removal Kit (Miltenyi Biotec, Inc.). Cells were incubated with 100 µL of dead cell removal microbeads at room temperature for 15 minutes, followed by magnetic separation using an MS column or the autoMACS Pro Separator. The eluted live cells were pelleted and resuspended in ice-cold PBS with 1% BSA.

In selected samples, 100 to 150 murine sarcoma cells (NIH/3T3 – CRL-1658, ATCC) were spiked into the final single-cell suspension to evaluate batch effects across processing sites. Approximately 8,000 cells were loaded per sample onto the 10x Genomics Chromium Controller, targeting the capture of up to 5,000 individual cells per sample. Reverse transcription, cDNA amplification, and library preparation were performed using the Chromium Next GEM Single Cell 3′ GEM, Library & Gel Bead Kit v2.1. During reverse transcription, full-length poly-A mRNA transcripts were barcoded with a 16-nucleotide cell barcode and a 10-nucleotide unique molecular identifier (UMI). The resulting cDNA was enzymatically fragmented and size-selected (~400 bp) for library construction following 10x Genomics' guidelines. Final library concentrations were quantified by qPCR (Kapa Biosystems) to ensure optimal cluster density for paired-end sequencing on the NovaSeq 6000 platform (Illumina). Sequencing was performed at a target depth of 25,000 to 50,000 reads per cell, yielding gene expression profiles representing approximately 1,000 to 4,000 transcripts per cell.

Summary of scRNA-seq Processing, Quality Control, and Clustering

scRNA-seq data were processed using Cell Ranger (v6.0.1, 10x Genomics, Inc.) to demultiplex sequencing reads into FASTQ files, align reads to the human reference genome (GRCh38), and generate gene-by-cell UMI count matrices. Empty droplets were identified and removed using DropletUtils (v1.14.2; ref. 59). Ambient RNA contamination was addressed using CellBender (v0.3.0; ref. 60). For quality control, cells with fewer than 1,000 UMIs, fewer than 200 detected genes, or more than 20% of UMIs mapping to mitochondrial genes were excluded using Seurat (61). To correct for batch effects arising from processing sites and shipment batches, Harmony (v0.1; ref. 62) was applied to the resulting cell embeddings and cluster assignments. Louvain clustering was then performed on the batch-corrected embeddings using Seurat's clustering function to group cells with similar transcriptomic profiles. Clusters were visualized using Uniform Manifold Approximation and Projection. Doublets were identified by flagging clusters with high predicted doublet proportions using three independent tools: DoubletFinder (63), Scrublet (v0.2.3; ref. 64), and Pegasus (v1.8.1, https://github.com/lilab-bcb/pegasus). Clusters enriched for doublets were identified when flagged by at least two of the three methods, using a false discovery rate threshold of <0.05 based on Fisher exact test. See the Supplementary Methods S1 for a detailed description of processing, quality control, and clustering methods.

Bulk RNA-seq, Whole-Genome Sequencing, and Clinical Data

Bulk RNA-seq, whole-genome sequencing, and clinical data were procured from the MMRF Research Gateway using the IA22 release. For analysis of bulk RNA-seq, the raw count and TPM files produced by the salmon (65) pipeline for bias-aware transcript quantification. For whole-genome sequencing, we used the copy number estimate files produced by the gatk (66) pipeline, SNV and indel files, and the SV files produced by manta (67). Fusion transcript files were produced by STAR-Fusion (RRID: SCR_025853). Clinical flat files were downloaded with the per patient file providing information on clinical covariates, the per patient visit file providing clinical parameters assessed at quarterly visits, the survival file providing PFS and OS data used in survival analyses, and the treatment regimen file providing information about lines of treatment and agents used.

Summary of Differential Abundance Analyses

To assess changes in cell type proportions over time (e.g., from baseline to first response) and how these changes differed between groups (e.g., induction vs. induction with ASCT), we applied linear mixed-effects models. The primary objective was to identify differences in temporal trends between groups. For instance, the model would highlight a cell type that increases from baseline to first response in the induction-only group while either decreasing, remaining stable, or changing at a significantly different rate in the induction + ASCT group. To achieve this, we modeled cell type/subcluster proportions as a function of time, the covariate of interest (e.g., treatment group), and their interaction, and patient identifiers were incorporated as random effects to adjust for interindividual variability. Additional fixed effects, such as age and sex, were included if they were found to be differ between groups of the tested covariate (such as between induction and induction and ASCT). See the Supplementary Methods S1 for a detailed description of these analyses.

Summary of Expression Analyses

To identify transcriptomic changes across time point and treatment categories, differential expression was executed using linear models in the limma package (68). An adjusted *P* value (*P*.adj) cut point of 0.05 was used for all comparisons. GSEA was conducted using the ReactomePA (69) and fgsea (RRID: SCR_020938) packages in R. TF activity was inferred using the decoupleR package (70). Cellular communication analyses were performed using the CellChat package (22). See the Supplementary Methods S1 for a detailed description of these analyses.

Summary of Ig Diversity Analyses

GSEA revealed that naïve B cells from patients with GMpfs were enriched for pathways related to activation and migration, whereas memory B cells were enriched for germinal center formation and isotype switching. Based on these findings, we hypothesized that increased proportions of naïve B cells following ASCT are associated with greater diversity in Ig expression across naïve and memory B cells. To test this hypothesis, we calculated the Shannon diversity index on Ig gene expression and correlated the resulting diversity scores with the $\log_2$ fold change in naïve B-cell proportion (first response vs. baseline). We additionally utilized the clinically assayed serum Ig measurements to corroborate the gene expression findings. Of the 1,143 patients included in the IA22 CoMMpass clinical metadata release, 408 met the following inclusion criteria (i): received a single ASCT, (ii) available PFS and OS data, and (iii) had complete clinical covariate information, including age, ISS stage at diagnosis, and induction regimen. These 408 patients were partitioned into derivation and validation cohorts, Shannon diversity index values were calculated based on their serum Ig values, and PFS/OS were compared between patients with high and low Shannon diversity values. See the Supplementary Methods S1 for a detailed description of these analyses.

Transcriptomic Analyses of Longitudinal CD138^{pos} Bulk RNA-seq Samples

To identify changes in gene expression from baseline to first progression, we performed differential expression analysis on 67 paired CD138^{pos} bulk RNA-seq samples. Statistical significance was determined using a moderated t-statistic with Benjamini–Hochberg correction for multiple testing, applying a significance threshold of 0.05. Given that CTAgs were found to be prominent among the top differentially expressed genes, we curated a list of candidate CTAgs from 14 publications and databases, yielding an initial pool of 575 genes (71–83). This list was then refined using the following criteria: (i) presence in at least two of the 14 sources, (ii) localization to the X chromosome to enrich for genes highly likely to be subject to epigenetic silencing in somatic tissues, (iii) inclusion in CTAg families with at least three members (e.g., *MAGE* genes) as these genes are typically found in close proximity on the X chromosome, and (iv) expression in fewer than 50% of CD138^{pos} bulk RNA-seq samples (TPM >1). To identify samples enriched for specific gene categories (i.e., CTAgs), we applied a gene module scoring by taking the average of log-transformed TPM values. See the Supplementary Methods S1 for a detailed description of these analyses.

Summary of Evaluation of Cytogenetic Alterations and Mutations in CD138^{pos} Whole-Genome Sequencing

To comprehensively evaluate genetic alterations including CNAs, SVs, fusion transcripts, and SNVs, we performed an integrative analysis similar to that described by Skerget and colleagues (37). For CNAs, we used the gene-by-sample matrix based on the lowest $\log_2$ segment mean in tumor samples relative to their matched normal (somatic) controls. For gene fusion detection, we utilized both StarFusion (RRID: SCR_025853) and PairoScope outputs to identify genes altered by fusion events. For SVs, we used the output files generated by the Manta pipeline (67). For SNVs, we applied a multilayered approach. To first inclusively identify SNVs, we used the gene-by-sample matrix of nonsynonymous SNV counts. Then, to further identify SNVs that occur frequently, we added two additional flags using the variant call format (VCF) files, following a method similar to Skerget and colleagues (37). First, we applied quality filters to retain SNVs with at least 10 reads in both tumor and reference samples, an allelic ratio above 0.05, detection by at least two of five variant callers (MUTECT2, STRELKA2, VARDICT, OCTOPUS, and LANCET), and a predicted impact of either "high" or "moderate." From this filtered VCF file, mutations were flagged as recurrent if the same amino acid alteration occurred in at least two patients or as clustered if at least five patients had nonsynonymous mutations within 10% of the coding DNA sequence of the gene. See the Supplementary Methods S1 for a detailed description of these analyses.

Summary of Subclonal Reconstruction

To infer subclonal progression of malignant cells across longitudinal samples, we performed subclonal reconstruction analysis on the CD138^{pos} whole-genome sequencing data from six patients who had three or more samples and progressive enrichment for CTAg genes. To account for CNAs, each SNV was assigned a copy number state based on the estimates produced by GATK. The thresholds for $\log_2$ segment mean values were derived from the theoretical value in which 80% of tumor cells would exhibit the given copy number. For instance, the threshold for monoallelic loss was set at −0.737, corresponding to the expected reads if 80% of the cells were monoploid and 20% were diploid. SNV clustering was performed using the One_step_clustering function in QuantumClone (84) with the "flash" preclustering method and clone rangers set from 1:2 to 1:4 to minimize the identification of subclones driven by fewer than 10 SNVs. Clonal models were generated using the infer.clonal.models function in the clonevol (85) package with 1,000 bootstrapped models. See the Supplementary Methods S1 for a detailed description of these analyses.

Data Availability

All the single-cell raw data, processed summary data, and clinical information are available under controlled access at MMRF's VLAB shared resource (https://mmrfvirtuallab.org). The MMRF requires the minimum qualifications for access: apply for access at https://mmrfvirtuallab.org and to meet the following minimum qualifications: (i) must be a permanent employee of their institution and at a level equivalent to a tenure-track professor, (ii) senior investigator that is overseeing laboratory or research program. If the access request is approved, usually within a week, investigators will receive an email with instructions for downloading the data. Alternatively, a Seurat R object with processed UMI counts and limited metadata can be accessed at Zenodo (10.5281/zenodo.15025566). Bulk RNA-seq, whole-genome sequencing, and clinical metadata are available through the MMRF Research Gateway (research.themmrf.org). Requests to access these data will be reviewed by the data access committee at MMRF, and data will be released under a data transfer agreement that will protect the identities of patients involved in the study. For additional inquiries, please email ImmuneAtlasNetwork@themmrf.org. This study did not generate new unique reagents.

Authors' Disclosures

R.G. Jayasinghe reports personal fees from MMRF outside the submitted work. J.J. Keats reports grants from the MMRF during the conduct of the study, as well as grants and personal fees from Illumina, Inc. and personal fees from Janssen Pharmaceutical outside the submitted work. A. Lagana reports grants from Bristol Myers Squibb outside the submitted work. D. Avigan reports grants from the MMRF during the conduct of the study, as well as grants from Kite and AbbVie, grants and other support from Pfizer, and other support from Arcellx, Regeneron, Parexel, and Chugaii outside the submitted work; in addition, D. Avigan has a patent for DC/Tumor Fusion Vaccine issued. H.J. Cho reports other support from the MMRF during the conduct of the study, as well as grants from Genentech, Bristol Myers Squibb, and Takeda outside the submitted work. L.B. Baughn reports other support from Genentech outside the submitted work. A.K. Nooka reports personal fees from AstraZeneca, Blue Earth Diagnostics, Cellectar Biosciences, GlaxoSmithKline, Janssen, KITE Therapeutics, ONK Therapeutics, OPNA, Pfizer, Perceptive Informatics LLC, Premier Research, and Sebia outside the submitted work. S. Lonial reports personal fees from Bristol Myers Squibb, Janssen, AbbVie, Novartis, Celgene, Takeda, Regeneron, Pfizer, Amgen, and GSK outside the submitted work and is a member of BOD TG Therapeutics with stock, no oncology indications or trials. S. Kumar reports consulting with no personal payment from AbbVie, Amgen, ArcellX, BeiGene, Bristol Myers Squibb, Carsgen, GSK, Janssen, K36, Moderna, Pfizer, Regeneron, Roche-Genentech, Sanofi, and Takeda and with personal payment from CVS Caremark, as well as BD Biosciences clinical trial support to institution from AbbVie, Amgen, AstraZeneca, Bristol Myers Squibb, Carsgen, GSK, Gracell Bio, Janssen, Oricell, Roche-Genentech, Sanofi, Takeda, and Telogenomics. M.K. Samur reports grants from the National Cancer Institute and Paola and Rodger Riney Foundation during the conduct of the study, as well as personal fees from K36, NCGM, and AbbVie outside the submitted work. I.S. Vlachos reports grants from the MMRF during the conduct of the study. S. Gnjatic reports personal fees from Taiho Pharmaceuticals and grants from Regeneron, Boehringer Ingelheim, Takeda, Celgene, Janssen R&D, and Bristol Myers Squibb outside the submitted work. M.K. Bhasin reports grants from the MMRF and Myeloma Solution Fund during the conduct of the study, as well as other support from Sanofi/Genetech outside the submitted work. No disclosures were reported by the other authors.

Authors' Contributions

D.J. Ohlstrom: Conceptualization, data curation, formal analysis, validation, methodology, writing–original draft, writing–review and editing. **W.C. Pilcher:** Conceptualization, data curation, formal analysis, methodology, writing–review and editing. **M.E. Michaud:** Conceptualization, formal analysis, writing–review and editing. **C. Acharya:** Conceptualization, formal analysis, project administration, writing–review and editing. **S. Satpathy:** Conceptualization, formal analysis, writing–review and editing. **E. Gonzalez-Kozlova:** Conceptualization, formal analysis, writing–review and editing. **R.G. Jayasinghe:** Conceptualization, formal analysis, writing–review and editing. **K. Ferguson:** Conceptualization, formal analysis, writing–review and editing. **H.L. Mumme:** Conceptualization, formal analysis, writing–review and editing. **S. Nanda:** Conceptualization, formal analysis, writing–review and editing. **Y. Song:** Conceptualization, formal analysis, writing–review and editing. **S. Mantrala:** Conceptualization, formal analysis, writing–review and editing. **D. Karagkouni:** Conceptualization, formal analysis, writing–review and editing. **J. Schulman:** Conceptualization, formal analysis, writing–review and editing. **N. Pabustan:** Conceptualization, writing–review and editing. **J. Vieira Dos Santos:** Conceptualization, formal analysis, writing–review and editing. **D.W. Sherbenou:** Conceptualization, supervision, writing–review and editing. **J.J. Keats:** Conceptualization, supervision, writing–review and editing. **A.M. Gout:** Conceptualization, supervision, project administration, writing–review and editing. **S. Foltz:** Conceptualization, supervision, project administration, writing–review and editing. **A. Lagana:** Conceptualization, formal analysis, supervision, project administration, writing–review and editing. **T. Kourelis:** Conceptualization, formal analysis, supervision, writing–review and editing. **R. Vij:** Conceptualization, supervision, writing–review and editing. **M.V. Dhodapkar:** Conceptualization, supervision, writing–review and editing. **D. Avigan:** Conceptualization, supervision, writing–review and editing. **H.J. Cho:** Conceptualization, supervision, writing–review and editing. **L.B. Baughn:** Conceptualization, supervision, writing–review and editing. **A.K. Nooka:** Conceptualization, supervision, writing–review and editing. **S. Lonial:** Conceptualization, supervision, writing–review and editing. **S. Kumar:** Conceptualization, supervision, writing–review and editing. **M.K. Samur:** Conceptualization, supervision, writing–review and editing. **I.S. Vlachos:** Conceptualization, supervision, writing–review and editing. **L. Ding:** Conceptualization, supervision, writing–review and editing. **S. Gnjatic:** Conceptualization, supervision, writing–review and editing. **G. Mulligan:** Conceptualization, supervision, project administration, writing–review and editing. **M.K. Bhasin:** Conceptualization, formal analysis, supervision, methodology, writing–original draft, project administration, writing–review and editing.

Acknowledgments

The authors would like to acknowledge funding support from the MMRF (M.K. Bhasin, S. Gnjatic, S. Nanda, D. Avigan, and I.S. Vlachos); Myeloma Solutions Fund (M.K. Bhasin, D.J. Ohlstrom, M.E. Michaud, and W.C. Pilcher); National Institutes of Health grants U24CA224319 (S. Gnjatic), U01DK124165 (S. Gnjatic), and P30CA196521 (S. Gnjatic); Paula C. and Rodger O. Riney Blood Cancer Research Fund (R. Vij, L. Ding); 5K12CA090628 (T. Kourelis); NCI U24CA211006 (L. Ding); U2CCA233303 (L. Ding); and NCI R01CA258776 (I.S. Vlachos).

Note

Supplementary data for this article are available at Blood Cancer Discovery Online (https://bloodcancerdiscov.aacrjournals.org/).

Received June 5, 2025; revised October 2, 2025; accepted December 8, 2025; posted first December 9, 2025.

REFERENCES

1. Padala SA, Barsouk A, Barsouk A, Rawla P, Vakiti A, Kolhe R, et al. Epidemiology, staging, and management of multiple myeloma. Med Sci (Basel) 2021;9:3.
2. Gulla A, Anderson KC. Multiple myeloma: the (r)evolution of current therapy and a glance into future. Haematologica 2020;105:2358–67.
3. Podar K, Leleu X. Relapsed/refractory multiple myeloma in 2020/2021 and beyond. Cancers (Basel) 2021;13:5154.
4. Bhatt P, Kloock C, Comenzo R. Relapsed/refractory multiple myeloma: a review of available therapies and clinical scenarios encountered in myeloma relapse. Curr Oncol 2023;30:2322–47.
5. Schavgoulidze A, Cazaubiel T, Perrot A, Avet-Loiseau H, Corre J. Multiple myeloma: heterogeneous in every way. Cancers (Basel) 2021;13:1285.
6. Pilcher W, Thomas BE, Bhasin SS, Jayasinghe RG, Yao L, Gonzalez-Kozlova E, et al. Cross center single-cell RNA sequencing study of the immune microenvironment in rapid progressing multiple myeloma. NPJ Genom Med 2023;8:3.
7. Zavidij O, Haradhvala NJ, Mouhieddine TH, Sklavenitis-Pistofidis R, Cai S, Reidy M, et al. Single-cell RNA sequencing reveals compromised immune microenvironment in precursor stages of multiple myeloma. Nat Cancer 2020;1:493–506.

8. Schinke C, Poos AM, Bauer M, John L, Johnson S, Deshpande S, et al. Characterizing the role of the immune microenvironment in multiple myeloma progression at a single-cell level. Blood Adv 2022;6:5873–83.
9. Parmar H, Gertz M, Anderson EI, Kumar S, Kourelis TV. Microenvironment immune reconstitution patterns correlate with outcomes after autologous transplant in multiple myeloma. Blood Adv 2021;5:1797–804.
10. Chung DJ, Pronschinske KB, Shyer JA, Sharma S, Leung S, Curran SA, et al. T-cell exhaustion in multiple myeloma relapse after autotransplant: optimal timing of immunotherapy. Cancer Immunol Res 2016;4:61–71.
11. Wang T, Fiala MA, Fortier JM, Liu R, Jayasinghe RG, Vij R, et al. Association between bone marrow immune microenvironment following autologous stem cell transplant and duration of response for multiple myeloma. Blood 2022;140:7066–7.
12. Díaz-Tejedor A, Lorenzo-Mohamed M, Puig N, García-Sanz R, Mateos M-V, Garayoa M, et al. Immune system alterations in multiple myeloma: molecular mechanisms and therapeutic strategies to reverse immunosuppression. Cancers (Basel) 2021;13:1353.
13. Witzens-Harig M, Hose D, Jünger S, Pfirschke C, Khandelwal N, Umansky L, et al. Tumor cells in multiple myeloma patients inhibit myeloma-reactive T cells through carcinoembryonic antigen-related cell adhesion molecule-6. Blood 2013;121:4493–503.
14. Liu J, Hamrouni A, Wolowiec D, Coiteux V, Kuliczkowski K, Hetuin D, et al. Plasma cells from multiple myeloma patients express B7-H1 (PD-L1) and increase expression after stimulation with IFN-{gamma} and TLR ligands via a MyD88-, TRAF6-, and MEK-dependent pathway. Blood 2007;110:296–304.
15. Wang C, Wang W, Wang M, Deng J, Sun C, Hu Y, et al. Different evasion strategies in multiple myeloma. Front Immunol 2024;15:1346211.
16. Rajkumar SV. Multiple myeloma: 2022 update on diagnosis, risk stratification, and management. Am J Hematol 2022;97:1086–107.
17. Johnson W, Bharel S, Sun M, Klumpp T, Hong J, Binder A, et al. Impaired CD4$^+$ T-cell recovery after autologous stem cell transplantation in patients with myeloma and lymphoma in the modern era. Biol Blood Marrow Transplant 2020;26:S311.
18. Liang Z, Dong X, Zhang Z, Zhang Q, Zhao Y. Age-related thymic involution: mechanisms and functional impact. Aging Cell 2022;21:e13671.
19. Van Den Brink MRM, Velardi E, Perales M-A. Immune reconstitution following stem cell transplantation. Hematology Am Soc Hematol Educ Program 2015;2015:215–9.
20. Bhat P, Leggatt G, Waterhouse N, Frazer IH. Interferon-γ derived from cytotoxic lymphocytes directly enhances their motility and cytotoxicity. Cell Death Dis 2017;8:e2836.
21. Refaeli Y, Van Parijs L, Alexander SI, Abbas AK. Interferon gamma is required for activation-induced death of T lymphocytes. J Exp Med 2002;196:999–1005.
22. Jin S, Guerrero-Juarez CF, Zhang L, Chang I, Ramos R, Kuan C-H, et al. Inference and analysis of cell-cell communication using CellChat. Nat Commun 2021;12:1088.
23. Mehta AK, Gracias DT, Croft M. TNF activity and T cells. Cytokine 2018;101:14–8.
24. Tze LE, Horikawa K, Domaschenz H, Howard DR, Roots CM, Rigby RJ, et al. CD83 increases MHC II and CD86 on dendritic cells by opposing IL-10–driven MARCH1-mediated ubiquitination and degradation. J Exp Med 2011;208:149–65.
25. Zhou Y, Wu H, Zhao M, Chang C, Lu Q. The Bach family of transcription factors: a comprehensive review. Clinic Rev Allerg Immunol 2016;50:345–56.
26. Zhao J, Bian ZC, Yee K, Chen BPC, Chien S, Guan J-L. Identification of transcription factor KLF8 as a downstream target of focal adhesion kinase in its regulation of cyclin D1 and cell cycle progression. Mol Cell 2003;11:1503–15.
27. Zhu H, Hu F, Sun X, Zhang X, Zhu L, Liu X, et al. CD16$^+$ monocyte subset was enriched and functionally exacerbated in driving T-cell activation and B-cell response in systemic lupus erythematosus. Front Immunol 2016;7:512.
28. Smulski CR, Eibel H. BAFF and BAFF-receptor in B cell selection and survival. Front Immunol 2018;9:2285.
29. Starlets D, Gore Y, Binsky I, Haran M, Harpaz N, Shvidel L, et al. Cell-surface CD74 initiates a signaling cascade leading to cell proliferation and survival. Blood 2006;107:4807–16.
30. Farhangnia P, Ghomi SM, Mollazadehghomi S, Nickho H, Akbarpour M, Delbandi A-A. SLAM-family receptors come of age as a potential molecular target in cancer immunotherapy. Front Immunol 2023;14:1174138.
31. Jenal M, Batliner J, Reddy VA, Haferlach T, Tobler A, Fey MF, et al. The anti-apoptotic gene BCL2A1 is a novel transcriptional target of PU.1. Leukemia 2010;24:1073–6.
32. Ereño-Orbea J, Sicard T, Cui H, Mazhab-Jafari MT, Benlekbir S, Guarné A, et al. Molecular basis of human CD22 function and therapeutic targeting. Nat Commun 2017;8:764.
33. Zhao M, Chauhan P, Sherman CA, Singh A, Kaileh M, Mazan-Mamczarz K, et al. NF-κB subunits direct kinetically distinct transcriptional cascades in antigen receptor-activated B cells. Nat Immunol 2023;24:1552–64.
34. Fratta E, Coral S, Covre A, Parisi G, Colizzi F, Danielli R, et al. The biology of cancer testis antigens: putative function, regulation and therapeutic potential. Mol Oncol 2011;5:164–82.
35. Van Duin M, Broyl A, De Knegt Y, Goldschmidt H, Richardson PG, Hop WCJ, et al. Cancer testis antigens in newly diagnosed and relapse multiple myeloma: prognostic markers and potential targets for immunotherapy. Haematologica 2011;96:1662–9.
36. Atanackovic D, Arfsten J, Cao Y, Gnjatic S, Schnieders F, Bartels K, et al. Cancer-testis antigens are commonly expressed in multiple myeloma and induce systemic immunity following allogeneic stem cell transplantation. Blood 2007;109:1103–12.
37. Skerget S, Penaherrera D, Chari A, Jagannath S, Siegel DS, Vij R, et al. Comprehensive molecular profiling of multiple myeloma identifies refined copy number and expression subtypes. Nat Genet 2024;56:1878–89.
38. Mittal SK, Cho K-J, Ishido S, Roche PA. Interleukin 10 (IL-10)-mediated immunosuppression: March-I induction regulates antigen presentation by macrophages but not dendritic cells. J Biol Chem 2015;290:27158–67.
39. Han F, Ma J. Pan-cancer analysis reveals IL32 is a potential prognostic and immunotherapeutic biomarker in cancer. Sci Rep 2024;14:8129.
40. Zhou C, Gao Y, Ding P, Wu T, Ji G. The role of CXCL family members in different diseases. Cell Death Discov 2023;9:212.
41. Lim HX, Hong H-J, Cho D, Kim TS. IL-18 enhances immunosuppressive responses by promoting differentiation into monocytic myeloid-derived suppressor cells. J Immunol 2014;193:5453–60.
42. Wang G-C, Zhou M, Zhang Y, Cai H-M, Chiang S-T, Chen Q, et al. Screening and identifying a novel M-MDSCs-related gene signature for predicting prognostic risk and immunotherapeutic responses in patients with lung adenocarcinoma. Front Genet 2023;13:989141.
43. Robert F, Hardy S, Nagy Z, Baldeyron C, Murr R, Déry U, et al. The transcriptional histone acetyltransferase cofactor TRRAP associates with the MRN repair complex and plays a role in DNA double-strand break repair. Mol Cell Biol 2006;26:402–12.
44. Dillingham CM, Cormaty H, Morgan EC, Tak AI, Esgdaille DE, Boutz PL, et al. KDM3A and KDM3B regulate alternative splicing in mouse pluripotent stem cells. iScience 2025;28:112612.
45. Zhou B, Wang L, Zhang S, Bennett BD, He F, Zhang Y, et al. INO80 governs superenhancer-mediated oncogenic transcription and tumor growth in melanoma. Genes Dev 2016;30:1440–53.
46. Williams JPC, Walport LJ. PADI6: what we know about the elusive fifth member of the peptidyl arginine deiminase family. Philos Trans R Soc Lond B Biol Sci 2023;378:20220242.
47. Serra F, Nieto-Aliseda A, Fanlo-Escudero L, Rovirosa L, Cabrera-Pasadas M, Lazarenkov A, et al. p53 rapidly restructures 3D chromatin organization to trigger a transcriptional response. Nat Commun 2024;15:2821.
48. Koziner B, Dengra C, Cisneros M, Glancszpigel R. Double-blind prospective randomized comparison of interferon gamma-1b versus placebo after autologous stem cell transplantation. Acta Haematol 2002;108:66–73.

49. González-Calle V, Cerdá S, Labrador J, Sobejano E, González-Mena B, Aguilera C, et al. Recovery of polyclonal immunoglobulins one year after autologous stem cell transplantation as a long-term predictor marker of progression and survival in multiple myeloma. Haematologica 2017;102:922–31.
50. Ozaki S, Harada T, Yagi H, Sekimoto E, Shibata H, Shigekiyo T, et al. Polyclonal immunoglobulin recovery after autologous stem cell transplantation is an independent prognostic factor for survival outcome in patients with multiple myeloma. Cancers (Basel) 2019;12:12.
51. John M, Helal M, Duell J, Mattavelli G, Stanojkovska E, Afrin N, et al. Spatial transcriptomics reveals profound subclonal heterogeneity and T-cell dysfunction in extramedullary myeloma. Blood 2024;144:2121–35.
52. Qi Y, Li H, Qi K, Zhu F, Cheng H, Chen W, et al. Clinical outcomes and microenvironment profiling in relapsed/refractory multiple myeloma patients with extramedullary disease receiving anti- BCMA CAR T-cell-based therapy. Am J Hematol 2024;99:2286–95.
53. Lutz R, Poos AM, Solé-Boldo L, John L, Wagner J, Prokoph N, et al. Bone marrow breakout lesions act as key sites for tumor-immune cell diversification in multiple myeloma. Sci Immunol 2025;10:eadp6667.
54. Lu Y, Yang A, Quan C, Pan Y, Zhang H, Li Y, et al. A single-cell atlas of the multicellular ecosystem of primary and metastatic hepatocellular carcinoma. Nat Commun 2022;13:4594.
55. Rasche L, Schinke C, Maura F, Bauer MA, Ashby C, Deshpande S, et al. The spatio-temporal evolution of multiple myeloma from baseline to relapse-refractory states. Nat Commun 2022;13:4517.
56. Heuck CJ, Qu P, Van Rhee F, Waheed S, Usmani SZ, Epstein J, et al. Five gene probes carry most of the discriminatory power of the 70-gene risk model in multiple myeloma. Leukemia 2014;28:2410–3.
57. Shaughnessy JD, Zhan F, Burington BE, Huang Y, Colla S, Hanamura I, et al. A validated gene expression model of high-risk multiple myeloma is defined by deregulated expression of genes mapping to chromosome 1. Blood 2007;109:2276–84.
58. Naik A, Lattab B, Qasem H, Decock J. Cancer testis antigens: emerging therapeutic targets leveraging genomic instability in cancer. Mol Ther Oncol 2024;32:200768.
59. Lun ATL, Riesenfeld S, Andrews T, Dao TP, Gomes T; Participants in the 1st Human Cell Atlas Jamboree, et al. EmptyDrops: distinguishing cells from empty droplets in droplet-based single-cell RNA sequencing data. Genome Biol 2019;20:63.
60. Fleming SJ, Chaffin MD, Arduini A, Akkad A-D, Banks E, Marioni JC, et al. Unsupervised removal of systematic background noise from droplet-based single-cell experiments using CellBender. Nat Methods 2023;20:1323–35.
61. Hao Y, Hao S, Andersen-Nissen E, Mauck WM, Zheng S, Butler A, et al. Integrated analysis of multimodal single-cell data. Cell 2021;184:3573–87.e29.
62. Korsunsky I, Millard N, Fan J, Slowikowski K, Zhang F, Wei K, et al. Fast, sensitive and accurate integration of single-cell data with Harmony. Nat Methods 2019;16:1289–96.
63. McGinnis CS, Murrow LM, Gartner ZJ. DoubletFinder: doublet detection in single-cell RNA sequencing data using artificial nearest neighbors. Cell Syst 2019;8:329–37.e4.
64. Wolock SL, Lopez R, Klein AM. Scrublet: computational identification of cell doublets in single-cell transcriptomic data. Cell Syst 2019;8:281–91.e9.
65. Patro R, Duggal G, Love MI, Irizarry RA, Kingsford C. Salmon provides fast and bias-aware quantification of transcript expression. Nat Methods 2017;14:417–9.
66. van der Auwera G, O'Connor BD. Genomics in the cloud: using Docker, GATK, and WDL in Terra. 1st edition. Sebastopol (CA): O'Reilly Media; 2020.
67. Chen X, Schulz-Trieglaff O, Shaw R, Barnes B, Schlesinger F, Källberg M, et al. Manta: rapid detection of structural variants and indels for germline and cancer sequencing applications. Bioinformatics 2016;32:1220–2.
68. Ritchie ME, Phipson B, Wu D, Hu Y, Law CW, Shi W, et al. Limma powers differential expression analyses for RNA-sequencing and microarray studies. Nucleic Acids Res 2015;43:e47.
69. Yu G, He Q-Y. ReactomePA: an R/Bioconductor package for reactome pathway analysis and visualization. Mol Biosyst 2016;12:477–9.
70. Badia-i-Mompel P, Vélez Santiago J, Braunger J, Geiss C, Dimitrov D, Müller-Dott S, et al. decoupleR: ensemble of computational methods to infer biological activities from omics data. Bioinform Adv 2022;2:vbac016.
71. Rajagopalan K, Mooney SM, Parekh N, Getzenberg RH, Kulkarni P. A majority of the cancer/testis antigens are intrinsically disordered proteins. J Cell Biochem 2011;112:3256–67.
72. Lee S-Y, Obata Y, Yoshida M, Stockert E, Williamson B, Jungbluth AA, et al. Immunomic analysis of human sarcoma. Proc Natl Acad Sci U S A 2003;100:2651–6.
73. Kobayashi S, Hiwasa T, Arasawa T, Kagaya A, Ishii S, Shimada H, et al. Identification of specific and common diagnostic antibody markers for gastrointestinal cancers by SEREX screening using testis cDNA phage library. Oncotarget 2018;9:18559–69.
74. Stenner-Liewen F, Luo G, Sahin U, Tureci O, Koslovski M, Kautz I, et al. Definition of tumor-associated antigens in hepatocellular carcinoma. Cancer Epidemiol Biomarkers Prev 2000;9:285–90.
75. Song M-H, Choi K-U, Shin D-H, Lee C-H, Lee S-Y. Identification of the cancer/testis antigens AKAP3 and CTp11 by SEREX in hepatocellular carcinoma. Oncol Rep 2012;28:1792–8.
76. Wang K, Xu X, Nie Y, Dai L, Wang P, Zhang J. Identification of tumor-associated antigens by using SEREX in hepatocellular carcinoma. Cancer Lett 2009;281:144–50.
77. Takashima M, Kuramitsu Y, Yokoyama Y, Iizuka N, Harada T, Fujimoto M, et al. Proteomic analysis of autoantibodies in patients with hepatocellular carcinoma. Proteomics 2006;6:3894–900.
78. Shi Y-Y, Wang H-C, Yin Y-H, Sun W-S, Li Y, Zhang C-Q, et al. Identification and analysis of tumour-associated antigens in hepatocellular carcinoma. Br J Cancer 2005;92:929–34.
79. Uemura M, Nouso K, Kobayashi Y, Tanaka H, Nakamura S, Higashi T, et al. Identification of the antigens predominantly reacted with serum from patients with hepatocellular carcinoma. Cancer 2003;97:2474–9.
80. Lee M-J, Yu G-R, Park S-H, Cho B-H, Ahn J-S, Park H-J, et al. Identification of cystatin B as a potential serum marker in hepatocellular carcinoma. Clin Cancer Res 2008;14:1080–9.
81. Chen G, Wang X, Yu J, Varambally S, Yu J, Thomas DG, et al. Autoantibody profiles reveal ubiquilin 1 as a humoral immune response target in lung adenocarcinoma. Cancer Res 2007;67:3461–7.
82. Zhang S, Liu Y, Chen J, Shu H, Shen S, Li Y, et al. Autoantibody signature in hepatocellular carcinoma using seromics. J Hematol Oncol 2020;13:85.
83. Stelzer G, Rosen N, Plaschkes I, Zimmerman S, Twik M, Fishilevich S, et al. The GeneCards suite: from gene data mining to disease genome sequence analyses. Curr Protoc Bioinformatics 2016;54:1.30.1–33.
84. Deveau P, Colmet Daage L, Oldridge D, Bernard V, Bellini A, Chicard M, et al. QuantumClone: clonal assessment of functional mutations in cancer based on a genotype-aware method for clonal reconstruction. Bioinformatics 2018;34:1808–16.
85. Dang HX, White BS, Foltz SM, Miller CA, Luo J, Fields RC, et al. ClonEvol: clonal ordering and visualization in cancer sequencing. Ann Oncol 2017;28:3076–82.